













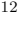













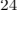











JWST-IPA: Chemical Inventory and Spatial Mapping of Ices in the Protostar HOPS370 – Evidence for an Opacity Hole and Thermal Processing of Ices

HIMANSHU TYAGI ¹, P. MANOJ ¹, MAYANK NARANG ^{2,1}, S. THOMAS MEGEATH ³, WILL R. M. ROCHA ⁴,
NASHANTY BRUNKEN ⁵, ADAM E. RUBINSTEIN ⁶, ROBERT GUTERMUTH ⁷, NEAL J. EVANS II ⁸,
EWINE F. VAN DISHOECK ^{5,9}, SAMUEL FEDERMAN ³, DAN M. WATSON ⁶, DAVID A. NEUFELD ¹⁰,
GUILLEM ANGLADA ¹¹, HENRIK BEUTHER ¹², ALESSIO CARATTI O GARATTI ¹³, LESLIE W. LOONEY ^{14,15},
POONEH NAZARI ⁵, MAYRA OSORIO ¹¹, THOMAS STANKE ⁹, YAO-LUN YANG ¹⁶, TYLER L. BOURKE ¹⁷,
WILLIAM J. FISCHER ¹⁸, ELISE FURLAN ¹⁹, JOEL GREEN ¹⁸, NOLAN HABEL ²⁰, PAMELA KLAASSEN ²¹,
NICOLE KARNATH ^{22,23}, HENDRIK LINZ ^{12,24}, JAMES MUZEROLLE ²⁵, JOHN J. TOBIN ¹⁵, PRABHANI ATNAGULOV ²⁶,
ROHAN RAHATGAONKAR ²⁷, PATRICK SHEEHAN ¹⁵, KATERINA SLAVICINSKA ⁵, AMELIA M. STUTZ ²⁸,
LUKASZ TYCHONIEC ²⁹ AND SCOTT WOLK ²³

¹*Department of Astronomy and Astrophysics Tata Institute of Fundamental Research
Homi Bhabha Road, Colaba, Mumbai 400005, India*

²*Academia Sinica Institute of Astronomy & Astrophysics,
11F of Astro-Math Bldg., No.1, Sec. 4, Roosevelt Rd., Taipei 10617, Taiwan*

³*University of Toledo, Toledo, OH, US*

⁴*Laboratory for Astrophysics, Leiden Observatory, Universiteit Leiden, Leiden, Zuid-Holland, NL*

⁵*Leiden Observatory, Universiteit Leiden, Leiden, Zuid-Holland, NL*

⁶*University of Rochester, Rochester, NY, US*

⁷*University of Massachusetts Amherst, Amherst, MA, US*

⁸*Department of Astronomy, The University of Texas at Austin, 2515 Speedway, Stop C1400, Austin, Texas 78712-1205, USA*

⁹*Max-Planck Institut für Extraterrestrische Physik, Garching bei München, DE*

¹⁰*William H. Miller III Department of Physics and Astronomy, The Johns Hopkins University, Baltimore, MD, USA*

¹¹*Instituto de Astrofísica de Andalucía, CSIC, Glorieta de la Astronomía s/n, E-18008 Granada, ES*

¹²*Max Planck Institute for Astronomy, Heidelberg, Baden Wuerttemberg, DE*

¹³*INAF-Osservatorio Astronomico di Capodimonte, IT*

¹⁴*Department of Astronomy, University of Illinois, 1002 West Green St, Urbana, IL 61801, USA*

¹⁵*National Radio Astronomy Observatory, 520 Edgemont Rd., Charlottesville, VA 22903 USA*

¹⁶*RIKEN Cluster for Pioneering Research, Wako-shi, Saitama, 351-0106, Japan*

¹⁷*SKA Observatory, Jodrell Bank, Lower Withington, Macclesfield SK11 9FT, UK*

¹⁸*Space Telescope Science Institute, 3700 San Martin Drive, Baltimore, MD 21218, US*

¹⁹*Caltech/IPAC, Pasadena, CA, US*

²⁰*Jet Propulsion Laboratory, Pasadena, CA, US*

²¹*United Kingdom Astronomy Technology Centre, Edinburgh, GB*

²²*Space Science Institute, Boulder, CO, US*

²³*Center for Astrophysics Harvard & Smithsonian, Cambridge, MA, US*

²⁴*Friedrich-Schiller-Universität, Jena, Thüringen, DE*

²⁵*Space Telescope Science Institute, Baltimore, MD, US*

²⁶*Ritter Astrophysical Research Center, Dept. of Physics and Astronomy, University of Toledo, Toledo, OH, US*

²⁷*Gemini South Observatory, La Serena, CL*

²⁸*Departamento de Astronomía, Universidad de Concepción, Casilla 160-C, Concepción, Chile*

²⁹*European Southern Observatory, Garching bei München, DE*

Submitted to ApJ

ABSTRACT

The composition of protoplanetary disks, and hence the initial conditions of planet formation, may be strongly influenced by the infall and thermal processing of material during the protostellar phase. Composition of dust and ice in protostellar envelopes, shaped by energetic processes driven by the protostar, serves as the fundamental building material for planets and complex organic molecules. As part of the JWST GO program, “Investigating Protostellar Accretion” (IPA), we observed an intermediate-mass protostar HOPS 370 (OMC2-FIR3) using NIRSpec/IFU and MIRI/MRS. This study presents the gas and ice phase chemical inventory revealed with the JWST in the spectral range of ~ 2.9 to $28 \mu\text{m}$ and explores the spatial variation of volatile ice species in the protostellar envelope. We find evidence for thermal processing of ice species throughout the inner envelope. We present the first high-spatial resolution (~ 80 au) maps of key volatile ice species H_2O , CO_2 , $^{13}\text{CO}_2$, CO , and OCN^- , which reveal a highly structured and inhomogeneous density distribution of the protostellar envelope, with a deficiency of ice column density that coincides with the jet/outflow shocked knots. Further, we observe high relative crystallinity of H_2O ice around the shocked knot seen in the H_2 and OH wind/outflow, which can be explained by a lack of outer colder material in the envelope along the line of sight due to the irregular structure of the envelope. These observations show clear evidence of thermal processing of the ices in the inner envelope, close to the outflow cavity walls, heated by the luminous protostar.

Keywords: Astrochemistry (75), Protostars (1302), Star formation (1569), Stellar jets (1607)

1. INTRODUCTION

Planetary systems are the natural byproducts of the star formation process (Hartmann 2009; Stahler & Palla 2004). Star formation begins with the collapse of a slowly rotating molecular cloud, followed by the formation of a central protostar and a circumstellar disk due to angular momentum conservation (Terebey et al. 1984; Hartmann 2009). The circumstellar disk serves as the birthplace of planets and is widely known as protoplanetary disk (Armitage 2020). Terrestrial planets, such as Earth, form in the inner disk regions, where temperatures are relatively high, resulting in planetesimals relatively depleted in volatiles. Yet, the Earth is enriched in volatiles relative to planetesimals in the inner disk (Morbidelli et al. 2012; van Dishoeck et al. 2014; Öberg & Bergin 2021).

How did the Earth get its volatile materials? Several studies (e.g., Morbidelli et al. 2012; Pontoppidan et al. 2014; Hartogh et al. 2011; Altwegg et al. 2019) suggest that comets and other icy bodies provided the Earth with much of its complement of volatiles. It is thought that comets are the most pristine objects in the solar system, and their chemical composition has not been altered since the solar protoplanetary disk stage (Mumma & Charnley 2011; Pontoppidan et al. 2014). This begs the question, is the chemical makeup of comets and the volatiles on Earth protoplanetary or interstellar in origin?

The debate over the origin centers around two main hypotheses: 1. chemical inheritance and evolution and 2. reset. Chemical inheritance refers to the idea that chemical composition is inherited from the molecular

cloud from which the protoplanetary disk is formed and should therefore be similar to the composition of the molecular cloud (Cleeves et al. 2014). In contrast, the reset hypothesis posits that the interstellar chemical composition is destroyed/reset and that the chemical inventory depends only on the chemical reactions taking place in the protoplanetary disks during the later stages of planet formation. The idea of reset is supported by meteoritic evidence (see for details Mumma & Charnley 2011; Pontoppidan et al. 2014). Moreover, several studies in the literature suggest contributions of both inheritance and reset (Brownlee et al. 2006; Visser et al. 2009; Ciesla 2010; Rubin et al. 2018; Drozdovskaya et al. 2019), but the relative importance of inheritance vs reset is poorly constrained (Öberg & Bergin 2021). However, the problem might not be dichotomous as intermediate stages of star formation, particularly the protostellar phase, undergo energetic events that might trigger chemical reactions to change the chemical makeup of the natal envelope.

The current epoch of star and planet formation within our Galaxy serves as a natural laboratory to understand the origin and formation mechanisms of our solar system and all planets more generally. Most importantly, the earliest phases of star formation can provide insights into the chemical evolution of the seed material for the stars and planets. The protostellar phase, often referred to as the primary accretion phase (Fischer et al. 2017; Narang et al. 2023; Federman et al. 2023; Tobin & Sheehan 2024), plays a vital role in accumulating/transporting gas and icy dust from the molecular cloud onto the star and the protostellar/protoplanetary

disk for planet formation (the birth-place of planets; see also Manara et al. 2018; Tychoniec et al. 2020). During this stage, most of the stellar mass is accreted (Fischer et al. 2017), and the initial conditions for planet formation are set. Hints of the early onset of planet formation, such as radial substructures detected by ALMA in protostellar disks, have also been seen during the protostellar phase (see e.g., ALMA Partnership et al. 2015; Sheehan & Eisner 2018; Sheehan et al. 2020; Segura-Cox et al. 2020; Ohashi et al. 2023). Further, simulations have shown that protostellar disks are more plausible sites for planetesimal formation than protoplanetary (Class II) disks because of their large gas and dust reservoirs (Tsukamoto et al. 2017; also see, Tanaka & Tsukamoto 2019).

While the protostellar phase plays a pivotal role in accretion, its impact on altering the chemical composition of dust and ice remains underexplored. Energetic processes occurring during this phase, such as luminosity of the protostar itself, particularly during accretion outbursts, UV emission from accretion and outflow shocks, shocks driven by jets/outflows, and X-rays from coronal activity, have the potential to significantly modify the physical structure and chemical composition of ice species within the natal envelope (e.g., Arce et al. 2008; Kim et al. 2012; Visser et al. 2015; Kim et al. 2022). Further, frequent accretion bursts can trigger and accelerate the formation reactions of complex organic molecules (COMs) in the envelope (Taquet et al. 2016). COMs have also been detected in the jet/outflow shocks from protostars (Arce et al. 2008; Codella et al. 2015; Lefloch et al. 2017). For a detailed discussion on chemistry during the protostellar phase, the reader is referred to Jørgensen et al. 2020; Öberg & Bergin 2021 and references therein. Therefore, it is important to understand the impact of these energetic processes in the protostellar phase in shaping the system’s chemistry.

The launch of the James Webb Space Telescope (JWST) has opened up the infrared spectral window rich in the spectral features of key volatile carriers, such as water (H_2O), carbon dioxide (CO_2), and carbon monoxide (CO), with a superior sensitivity and angular resolution compared to *ISO* and *Spitzer*. In particular, the Integral Field Units of Near InfraRed Spectrograph (NIRSpec; Böker et al. 2022; Jakobsen et al. 2022) and Mid-Infrared Instrument (MIRI; Rieke et al. 2015; Wright et al. 2015) offer a unique opportunity not only to investigate the chemical composition of a protostellar envelope but also to observe the spatial variations in its distribution. This technological advancement has paved the way for a spatial investigation of protostellar pro-

cesses that could shape/change the chemistry of volatiles within the envelope.

Investigating Protostellar Accretion (IPA) across the mass spectrum is a JWST Cycle 1 medium GO program (PID: 1802; P.I.: S Thomas Megeath; Megeath et al. 2021; Federman et al. 2024; Narang et al. 2024; Rubinstein et al. 2023; Neufeld et al. 2024, ; Watson et al. in prep) to observe five protostars in a broad luminosity range ($L_{\text{bol}} \sim 0.2 - 10^4 L_{\odot}$). IPA uses NIRSpec/IFU and MIRI/MRS in 2×2 mosaicing mode to obtain spectral cubes with a field of view of $6'' \times 6''$. The program aims to study protostellar accretion, jets/outflows (Federman et al. 2024; Narang et al. 2024), and to characterize the chemical properties of the protostellar environment (Brunken et al. 2024; Nazari et al. 2024; Slavicinska et al. 2024). Other programs with JWST have also focused on the icy chemistry (Yang et al. 2022; McClure et al. 2023; Rocha et al. 2024) and mass accretion/ejection processes of the protostars (Beuther et al. 2023; Francis et al. 2024; Tychoniec et al. 2024).

In this study, we investigate the spatial distribution of ice species and evidence for thermal processing within the envelope of the intermediate-mass protostar HOPS 370 (aka OMC2-FIR3), which is the second most luminous source in the IPA sample. It is a Class 0/I intermediate-luminosity protostar with a bolometric luminosity (L_{bol}) of $315.7 L_{\odot}$ (total luminosity $\sim 511 L_{\odot}$) and a bolometric temperature (T_{bol}) of 71.5 K (Furlan et al. 2016; Tobin et al. 2020a). The central protostar is deeply embedded in the envelope. It is located at a distance of 390 pc in the northern part of the Integral Shaped Filament (ISF) in the OMC-2 region with close to an edge-on geometry (inclination angle $\sim 71^\circ$; Federman et al. 2023; Tobin et al. 2020a,b). Multi-wavelength observations have revealed the presence of a strong bipolar jet/outflow (see e.g., Federman et al. 2024; Osorio et al. 2017; González-García et al. 2016; Takahashi et al. 2008). Our JWST observations have revealed the presence of a shocked knot in the northern part of the protostellar jet (see Federman et al. 2024; Neufeld et al. 2024).

In this paper, we present the chemical inventory of gas and ice species and map the spatial distribution of volatile ice species present in the envelope of HOPS 370. We also search for evidence of thermal processing of ice species in the protostellar envelope. In section 2, we discuss the observation and data reduction. In section 3, we present the observational results for HOPS 370. In section 4, we delve into an in-depth discussion of the findings and their implications and summarize our findings in section 5.

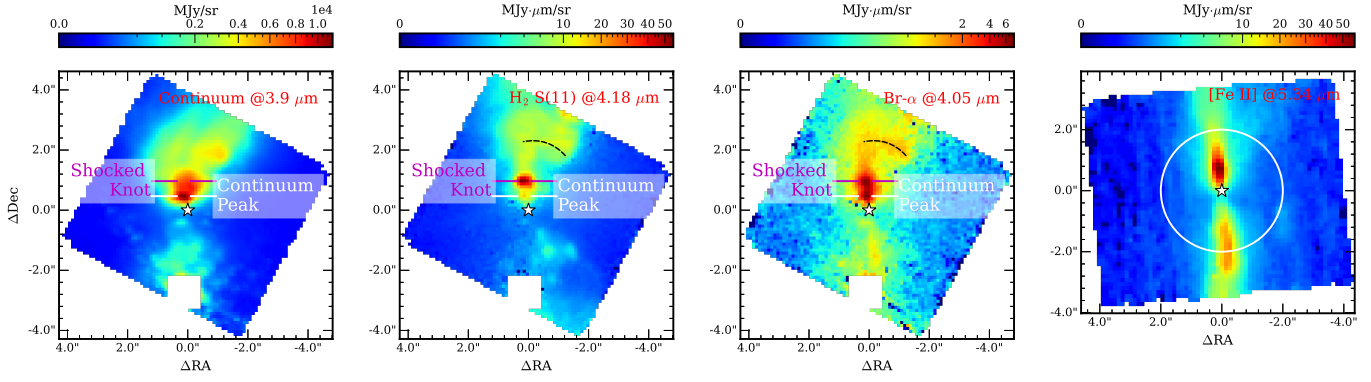


Figure 1. Morphology of the HOPS 370 protostellar environment seen in the continuum map at $3.9 \mu\text{m}$, H_2 S(11) map at $4.18 \mu\text{m}$, Br- α map at $4.05 \mu\text{m}$, and [Fe II] map at $5.34 \mu\text{m}$. All the line maps are continuum subtracted. The white star marks the ALMA continuum position in all the panels. The white circular aperture in the right panel is used for 1D spectrum extraction. The locations of the continuum peak and the shocked knot are shown using the horizontal white and magenta color lines, respectively. The dashed black line in the middle panels marks the fish hook-like structure in Br- α and H_2 . The bright foreground pre-main sequence star, [MGM2012] 2301, is masked to enhance the contrast.

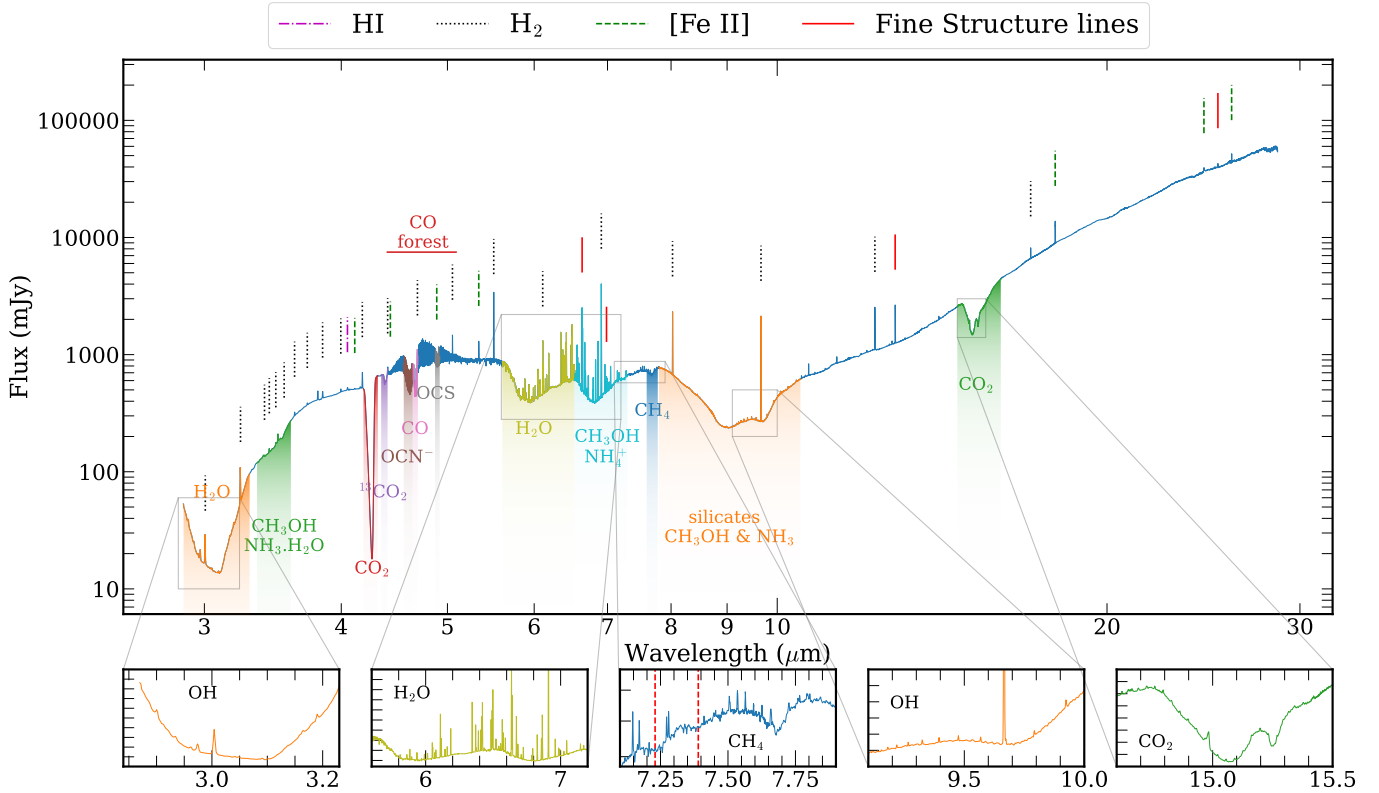


Figure 2. The extracted 1D spectrum using a $2''$ aperture centered at the ALMA continuum position of HOPS 370. Prominent absorption features are gradient-shaded in colors while the detected emission lines are marked using vertical line markers. Molecular lines of H_2O , CH_4 , OH, and CO_2 are displayed in the insets.

2. OBSERVATIONS AND DATA REDUCTION

The NIRSPEC IFU observations of HOPS 370 were carried out on October 16, 2022, using the F290LP/G395M filter/grating ($R \sim 700$ to ~ 1300). The spectral coverage for these observations is $\sim 2.87 - 5.01 \mu\text{m}$. Employ-

ing a 2×2 mosaicing mode with a 10% overlap and a 4-point-dither pattern, we achieved a $6'' \times 6''$ field of view (FOV). Given HOPS 370's brightness, we employed the NRSIRS2RAPID readout pattern, incorporating 15 groups per integration and 1 integration. The effec-

tive exposure time for these observations amounted to 3501.3 s.

The raw data obtained from the Mikulski Archive for Space Telescopes (MAST) was reduced using JWST pipeline version 1.9.5.dev7+gbf7d3c9b and CRDS context files ‘jwst_1069.pmap’. To achieve science-ready products we applied custom bad pixel masks and astrometry corrections. For further details regarding the data reduction and astrometry refinement processes, the reader is referred to [Federman et al. \(2024\)](#).

HOPS 370 was observed on March 15, 2023, with MIRI/MRS, in all four channels covering a spectral range from $\sim 4.9 \mu\text{m}$ to $28 \mu\text{m}$ at spectral resolving power ranging from $R \sim 4000$ to 1500 ([Jones et al. 2023](#)). Mosaicing settings for these observations were similar to those of NIRSpec with the 4-point-dither pattern. In MIRI observations, we have incorporated 50 groups per integration and 2 integrations with the FASTR1 read-out pattern. The effective exposure time for these observations was 4484.5 s. Dedicated observation of background with similar exposure parameters was also taken for background subtraction. The data reduction process for MIRI/MRS is discussed in [Neufeld et al. 2024](#).

Our FOVs (NIRSpec and MIRI) of HOPS 370 also include another source, [MGM2012] 2301 ([Megeath et al. 2012](#)), towards the south of HOPS 370.

3. RESULTS

The spectral images obtained using NIRSpec and MIRI reveal the gas and dust structure of the inner 1200 au surrounding the protostar and its chemical richness ([Federman et al. 2024](#); [Rubin et al. 2023](#); [Neufeld et al. 2024](#)). We present the chemical inventory and spatial ice distribution in this section.

3.1. Morphology

Figure 1 shows the continuum and line maps of HOPS 370 that reveal the morphology of the inner protostellar environment. The star symbol in all the panels of Figure 1 marks the ALMA continuum disk position ($05^{\text{h}}35^{\text{m}}27.63^{\text{s}} - 05^{\circ}09'34.42''$ (ICRS); [Tobin et al. 2020b](#)). The highly inclined orientation (approximately 72° inclination; [Tobin et al. 2020a](#); [Federman et al. 2024](#)) reveals the presence of an hourglass-shaped scattered-light cavities with the northern cavity brighter relative to the southern cavity (Figure 1, left panel). The northern cavity shows an east-west asymmetry with brighter emission to the west. Bright structured emission in H_2 is surrounded by a weaker hourglass-shaped H_2 emission (middle-left panel). In the northern cavity, a shocked knot is detected in both OH and H_2 (see also [Federman et al. 2024](#); [Neufeld et al. 2024](#)). The shocked knot is

$\sim 0.5''$ north of the scattered continuum peak (see Figure 1). The Br-Alpha line peaks at the shock knot and the continuum source (middle-right panel). There is a fish hook-like structure in Br- α and H_2 emission in the northern cavity ($\sim 2''$ away from the ALMA continuum position). A highly collimated jet is traced in [FeII] at $5.34 \mu\text{m}$, this also peaks at the position of the shock knot (right panel; see also [Federman et al. 2024](#); [Neufeld et al. 2024](#)). This collimated jet is also seen in Br-alpha and, in the northern cavity, H_2 ([Federman et al. 2024](#)).

3.2. The Chemical Inventory

In Figure 2, we present the combined NIRSpec and MIRI spectrum extracted from a $2''$ radius aperture centered on the ALMA continuum peak (see Figure 1). This spectrum covers the wavelength range from $2.87 \mu\text{m}$ to $28 \mu\text{m}$ and reveals a rich chemical inventory in both the gas and ice phases.

3.2.1. Gas Species

HOPS 370 shows a diverse set of gas-phase molecular emission lines. We detect many ro-vibrational lines from the P and R branches of CO that exhibit both extended and jet-like structures ([Rubin et al. 2023](#); [Federman et al. 2024](#)). Pure rotational lines of H_2 are marked in dotted black vertical lines in Figure 2. We have detected pure rotational H_2 lines from S(1) to S(19). The H_2 lines appear to have originated both in the jet and its warm gas in the cavity, with emission peaking at the shock knot (Figure 1; see also [Neufeld et al. 2024](#); [Federman et al. 2024](#); [Tyagi et al. in prep.](#)). We have also detected H_2O , OH, CH_4 , and CO_2 line forests, zoomed in the inset in Figure 2 (details about these lines will be discussed in [Manoj et al. in prep.](#), [Neufeld et al. in prep.](#), and [Rubin et al. in prep.](#), see also [Neufeld et al. 2024](#); [Francis et al. 2024](#)). The HCN ro-vibrational lines from P, Q, and R branches between the wavelength range of 13.7 to $14.3 \mu\text{m}$ are also detected. Further, we detect HI, [Fe II], and other fine-structure emission lines (see Figure 2). Detailed line lists of detected molecular and atomic/ionic species are given in Table A1 & A2, respectively. In Table A1, we do not present lines of CO, nor the lines at NIRSpec wavelengths as they have been already presented by [Rubin et al. 2023](#), and [Federman et al. 2024](#).

3.2.2. Ice Species

Many ice absorption features, highlighted in Figure 2, are detected at high signal-to-noise ratios (SNR). Dominant ice absorption features in the HOPS 370 spectrum include the OH stretching mode of H_2O at $3.0 \mu\text{m}$, CO_2 stretching mode at $4.27 \mu\text{m}$, $^{13}\text{CO}_2$ stretching mode at $4.38 \mu\text{m}$ ([Brunken et al. 2024](#)), OCN^- at $4.62 \mu\text{m}$, CO

stretching mode at $4.67 \mu\text{m}$, C-O stretch mode of OCS at $4.90 \mu\text{m}$, H₂O bending mode at $6.0 \mu\text{m}$, CH₃OH/NH₄⁺ at $6.85 \mu\text{m}$, CH₄ at $7.67 \mu\text{m}$, and double-peaked CO₂ bending mode at $15.2 \mu\text{m}$. We detected the $9.7 \mu\text{m}$ silicate absorption feature blended with the NH₃ umbrella and CH₃OH absorption features. We also detected two weak absorption features at 7.23 and $7.38 \mu\text{m}$ probably due to C-H deformation bands of C₂H₅OH/HCOOH, and CH₃CHO/HCOO⁻ respectively (marked by red dashed lines in the third inset of the bottom row in Figure 2; also see Boogert et al. 2015; Rocha et al. 2024 for detailed discussion on these species). Absorption bands of NH₃:H₂O, CH₃OH at $\sim 3.5 \mu\text{m}$, and HDO ice at $\sim 4.1 \mu\text{m}$ have also been detected (Slavicinska et al. 2024). Additionally, we have a tentative detection of CH₃CN and C₂H₅CN (Nazari et al. 2024).

The presence of a narrow absorption feature at $3.1 \mu\text{m}$ due to crystalline H₂O and a double-peaked $15.2 \mu\text{m}$ CO₂ absorption feature suggests hints of thermal processing (Boogert et al. 2015). Furthermore, a double-peaked ¹³CO₂ absorption feature, attributed to ice segregation due to thermal processing, was observed by Brunken et al. (2024). However, the origin of thermal processing remains unclear based on the spectrum at a single position.

3.3. Spatial Variation of Ice Spectra

The 1D NIRSpec+MIRI spectrum, centered on the protostellar position, in Figure 2 shows signs of thermal processing, prompting further investigation into its localization and physical origin. IFU observations offer a comprehensive dataset for this investigation, particularly in the NIRSpec observation, where extended scattered light provides an extended background continuum to be absorbed by the ice species present in the protostellar envelope (see Figure 1, first panel from left).

To investigate the spatial variations in absorption features of ice species, we extract spectra at various positions in the protostellar envelope using circular apertures with a radius of $0.6''$. Our extraction apertures are displayed in Figure 3 overlaid on the $3.9 \mu\text{m}$ continuum image (referenced by numbers and colors in the top right panel). Extracted spectra, plotted in the sub-panels, share the same color as its extraction aperture in the right top panel. The overall spectra look qualitatively similar in all the apertures with some minor changes in absorption features, indicating that the dominant absorption ice species are common throughout the envelope.

The heating of CO₂ ice mixtures in the envelope can sublimate the most volatile ice species (distillation) and rearrange molecular bonds (segregation), which leads to

the formation of pure CO₂ ice (double-peaked absorption in the 4.38 and $15.2 \mu\text{m}$ feature indicates segregation/distillation of CO₂; see also, Ehrenfreund et al. 1997; Boogert et al. 2000; Pontoppidan et al. 2008). In our observations, ¹³CO₂ (displayed in the insets in Figure 3) also shows double-peaked absorption in all the apertures, suggesting CO₂ ice distillation/segregation due to thermal processing throughout the envelope. Apertures 0, 1, 2, and 3 show the absorption peak at $3.1 \mu\text{m}$ due to crystalline H₂O. Further, we detect a relatively weaker $4.67 \mu\text{m}$ CO absorption with respect to $4.27 \mu\text{m}$ CO₂ absorption feature in all the apertures. All the signatures of ice absorption features suggest that the protostellar envelope has undergone thermal processing.

3.4. Optical Depth Maps

To investigate the spatial distribution of the ice species, we generated peak optical depth maps from the NIRSpec observations (Figures 4 and 5). We first subtracted all the emission lines from the data cube and generated a line-free spectral cube (for details, see Rubinstein et al. 2023), which is then used to generate optical depth maps.

Next, we fitted a local continuum using low-order (2nd order for ¹³CO₂, CO, and OCN⁻; 4th order for CO₂) polynomials to the ice absorption features (except H₂O) at each spaxel. Local continua are used because scattering can produce large wing emissions, e.g., the blue wing of $4.27 \mu\text{m}$ CO₂ (Dartois et al. 2022, 2024), which makes fitting a global continuum challenging. Determining the continuum for H₂O at $3.0 \mu\text{m}$ poses additional challenges due to incomplete spectral coverage short ward of $2.87 \mu\text{m}$ of our observations. To address this, a straight-line fit is applied between anchor points at $4 \mu\text{m}$ to $4.18 \mu\text{m}$ and $\sim 2.87 \mu\text{m}$. While fitting a straight line continuum using an anchor point at $2.87 \mu\text{m}$ for the H₂O may underestimate the true optical depth, it facilitates comparison of relative strengths across the IFU. We calculated the optical depth at each spaxel using the following equation,

$$\tau_\lambda = -\ln \left[\frac{I_{\lambda,obs}}{I_{\lambda,cont}} \right] \quad (1)$$

here, $I_{\lambda,obs}$ is the observed specific intensity value and $I_{\lambda,cont}$ is the continuum estimated from the fit.

Figure 4 illustrates the results of optical depth calculations for CO₂ at $4.27 \mu\text{m}$. The left panel shows the peak optical depth map. The middle and right panels showcase spectral profiles with fitted continuum and the corresponding optical depth, respectively, for spaxels marked with crosses on the optical depth map.

The peak optical depth maps of other species (H₂O at $3.0 \mu\text{m}$, ¹³CO₂ at $4.38 \mu\text{m}$, CO at $4.67 \mu\text{m}$, and OCN⁻

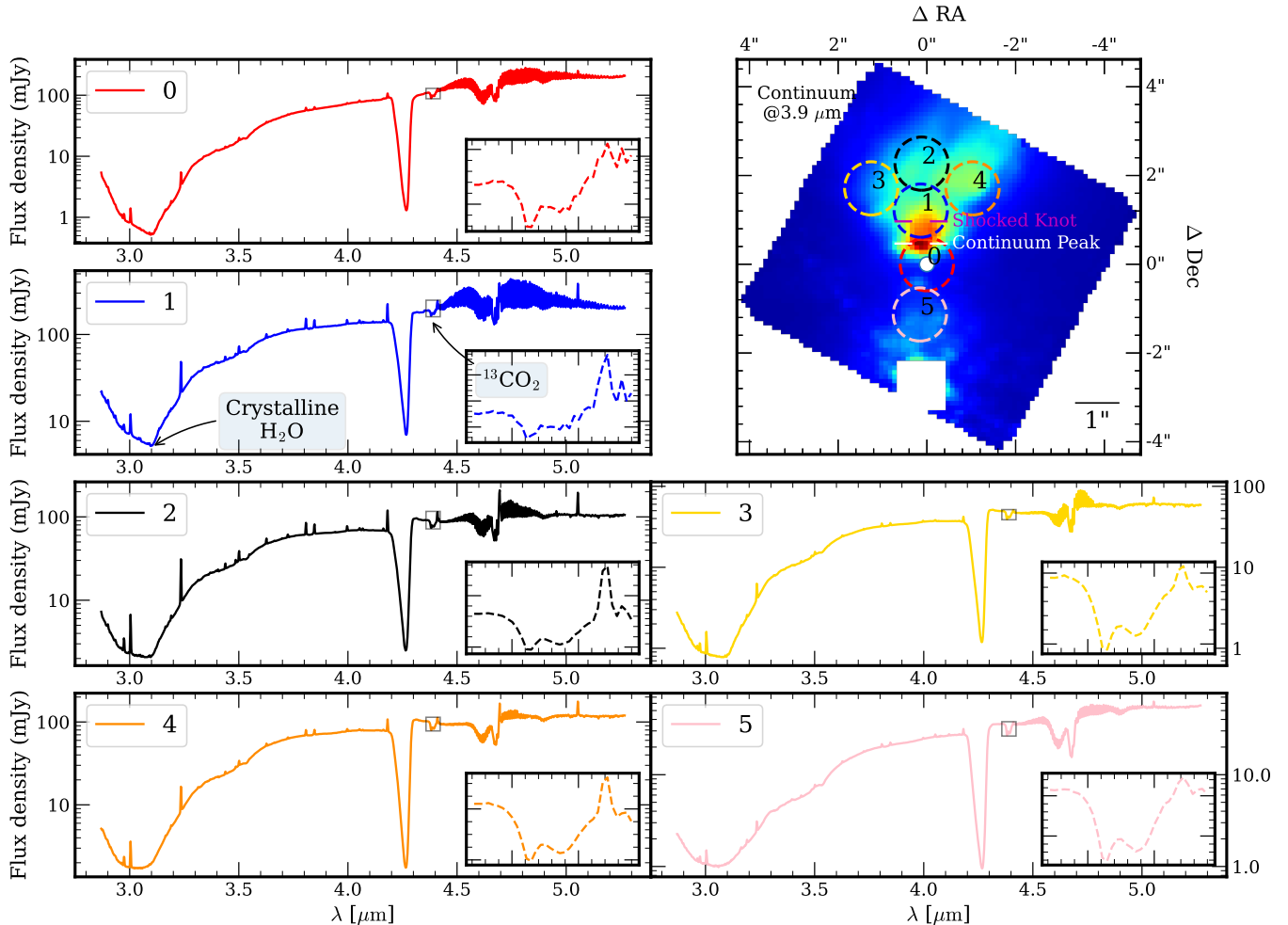


Figure 3. Spatial variation of the NIRSPEC spectrum extracted from the circular apertures of $0.6''$ radius that are shown overlaid on the $3.9 \mu\text{m}$ continuum image. The numbers and colors corresponding to apertures are used to point to the extracted spectrum. Other color schemes are similar to Figure 1. Insets in the spectra panels display the $^{13}\text{CO}_2$ ice feature. The [MGM2012] 2301 is masked in the continuum image to enhance the contrast.

at $4.61 \mu\text{m}$) are shown in Figure 5. Peak optical depth maps of all the species show more or less similar morphology and exhibit a low optical depth region around the shocked knot (roughly $0.8''$, (~ 312 au) north of the ALMA continuum position). There is another extended low optical depth region $\sim 2''$ (~ 780 au) northwest of the ALMA continuum position, separated by a band of extinction. A relatively high optical depth region is located at the scattered light continuum peak, indicating a change in scattered light emission structure at the peak ice absorption wavelength. Additionally, we find another high optical depth region, northwest of the ALMA continuum position off the edge of the outflow cavity (near $\Delta\text{RA}, \Delta\text{Dec} = -2.0'', 2.0''$).

In the southern part of the FOV, spatial information is obscured by the PSF artifacts due to [MGM2012] 2301, a bright pre-main sequence star saturated at NIRSPEC wavelengths (see also Federman et al. 2024). However,

the $^{13}\text{CO}_2$ and CO maps (top-right and bottom-left panels of Figure 5, respectively), which are relatively less affected by artifacts, suggest an increase in optical depth, roughly following an hourglass geometry in the southern envelope similar to scattered light.

In summary, the optical depth maps of the ice species examined show similar spatial structures in the northern cavity (see Figures 4 and 5), suggesting a common origin for these structures.

3.5. Low Extinction around Shocked Knot

Motivated by the low optical depth regions highlighted in Figures 4 and 5, we further investigated the scattered light emission across the FOV at the peak CO_2 ice absorption wavelength ($4.27 \mu\text{m}$), as illustrated in Figure 6. We use mean channel maps to compare the observed intensity structures at the ice absorption-free continuum and peak ice absorption wavelengths.

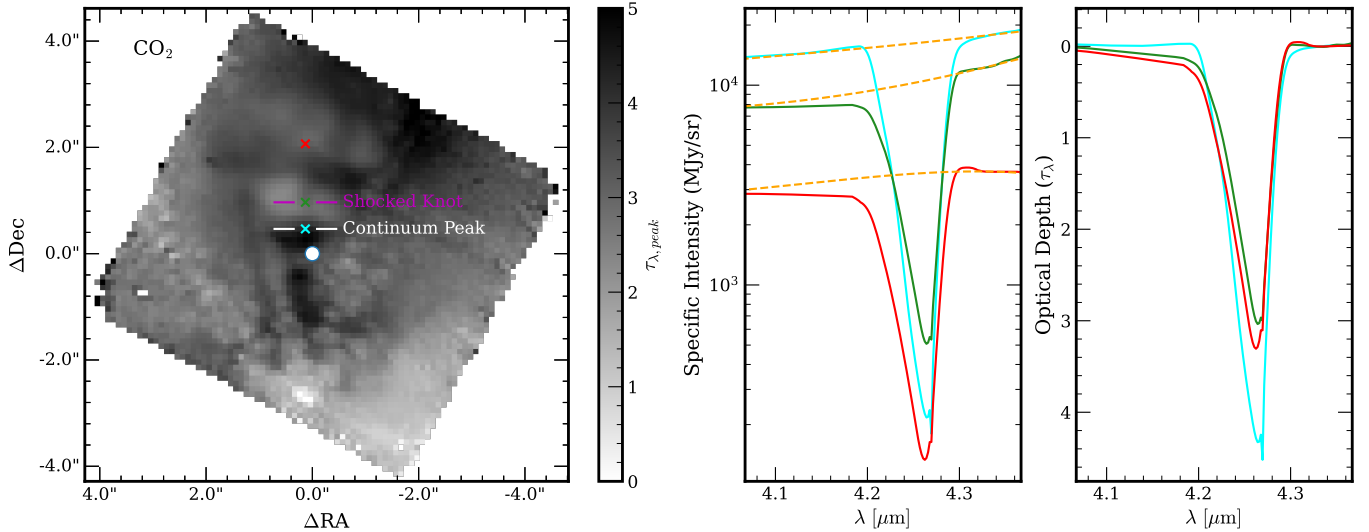


Figure 4. Peak optical depth map of CO_2 and illustration of optical depth calculation for each spaxel. *Left:* Peak optical depth map of CO_2 at $4.27 \mu\text{m}$, with the white circle indicating the ALMA $870 \mu\text{m}$ continuum peak. Cyan, green, and red crosses mark spaxel positions corresponding to the fit results displayed in the middle and right panels. *Middle:* Specific intensity of marked spaxel (‘x’) as a function of wavelength. The colors of the plotted lines correspond to the same color ‘x’ spaxel. The dashed orange lines represent the fitted continuum to the respective spaxel. *Right:* Calculated optical depths for the marked spaxels.

In Figure 6, the left and right column panels display the mean channel maps at ice absorption-free wavelengths on the blue and red sides of the $4.27 \mu\text{m}$ CO_2 , respectively. The middle panel in the top row displays the observed mean channel map at the peak ice absorption wavelengths. Moreover, red-shaded regions overlaid on the extracted spectrum below each map highlight the spectral regions corresponding to the displayed mean channel maps.

The scattered light continuum in the left and right panels in Figure 6 show similar hourglass geometry with the northern part being brighter. The emission peaks in both panels are marked by white horizontal bars. However, the emission structure in the middle panel differs significantly from the left and right panels, showing a shifted emission peak and disappearance of the hourglass geometry.

A similar change in the observed intensity structures at the peak ice absorption wavelengths compared to the scattered continuum is seen for all the ice species (also evident from the optical depth maps in Figure 5), suggesting that all the scattered light in FOV except at the shocked knot position is getting significantly absorbed at peak ice absorption wavelengths, and only the light at the shocked knot position escapes the protostellar envelope at those wavelengths.

3.6. Mapping the Excess Crystallization of Water Ice

To investigate the region of excess heating as indicated and discussed in Section 3.3, we map the ratio

between crystalline and amorphous H_2O ice within the FOV. This was done by following the procedure discussed in Section 3.4. Initially, optical depth maps were generated at $3.0 \mu\text{m}$ (the peak absorption wavelength for amorphous H_2O) and $3.1 \mu\text{m}$ (the peak absorption wavelength for crystalline H_2O). The ratio of the optical depth map at $3.1 \mu\text{m}$ to that at $3.0 \mu\text{m}$ then, is a measure of excess absorption due to crystalline H_2O . Figure 7 shows the ratio map, clearly indicating that the ratio is higher toward the shocked knot, with the highest water crystallization coincident with the shocked knot. The southern part of the ratio map is noisy due to the PSF artifacts of [MGM2012] 2301.

3.7. Spatial Decomposition Maps of $^{13}\text{CO}_2$, OCN^- and CO

To further investigate the envelope environment, we show the decomposed maps of $^{13}\text{CO}_2$, OCN^- , and CO in Figures 8. The decomposed maps are generated by fitting the observed absorption features using laboratory spectra of contributing species in the respective ice absorption bands. These maps cover the inner $4'' \times 4''$ region.

To generate the decomposed maps, the $4'' \times 4''$ region was divided into a 2D grid with a cell size of 3 pixel \times 3 pixels ($\sim 0.3'' \times 0.3''$). This binning approach, employed instead of utilizing individual pixels, enhances the SNR for subsequent decomposition analysis. Spectra were extracted from each $0.3'' \times 0.3''$ square cell. Subsequently, we fit a low-order (3rd order for $^{13}\text{CO}_2$; 2nd order for

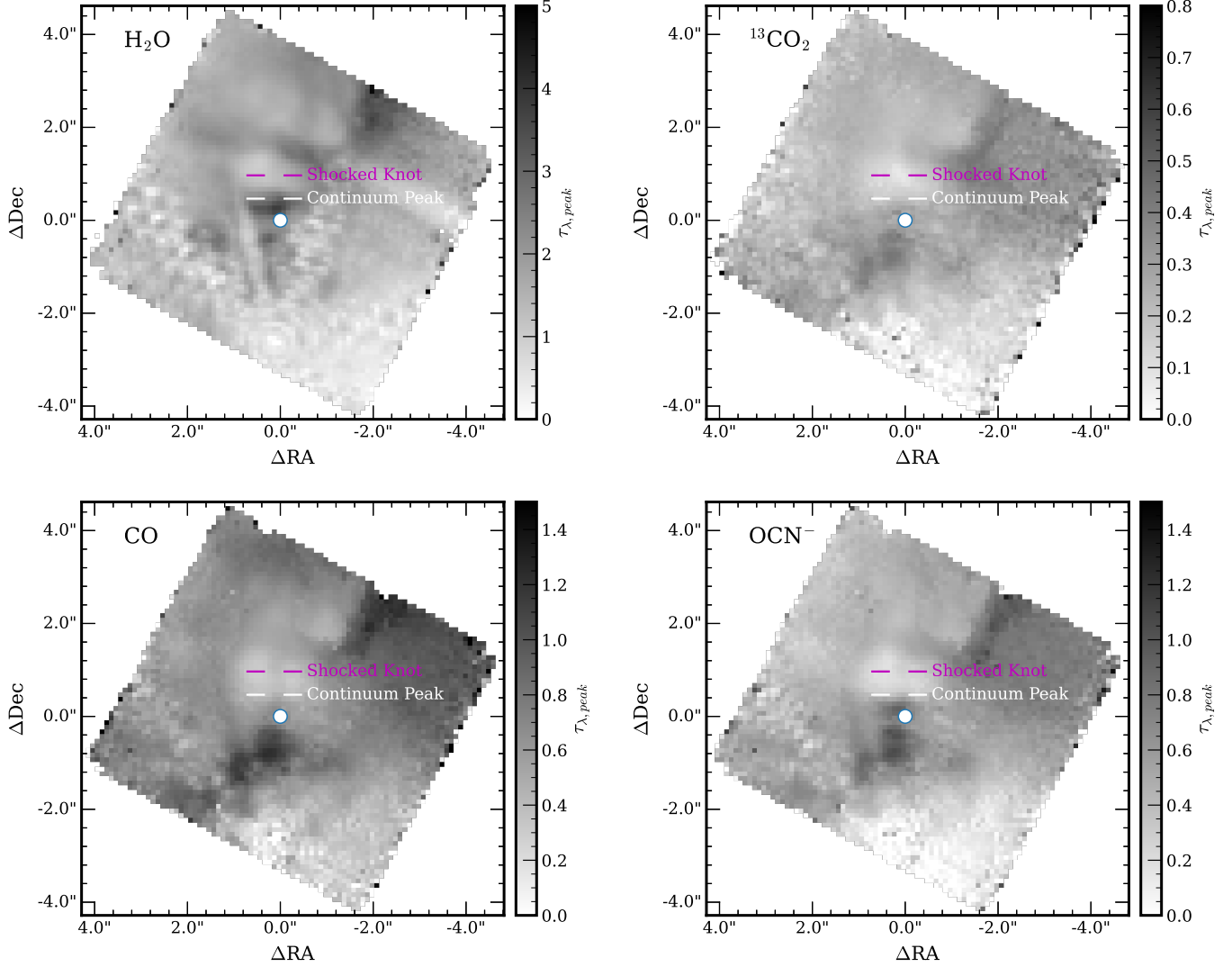


Figure 5. Peak optical depth map of H_2O at $3.0 \mu\text{m}$, $^{13}\text{CO}_2$ at $4.38 \mu\text{m}$, CO at $4.67 \mu\text{m}$, and OCN^- at $4.61 \mu\text{m}$. The white circle marks the ALMA continuum position. The southern region of all the maps is affected by the PSF artifacts of [MGM2012] 2301.

CO and OCN^-) polynomial local continuum in the extracted spectra to obtain the optical depths for each cell. These derived optical depth values were then used in the decomposition of the absorption features.

For the decomposition of $^{13}\text{CO}_2$, we followed the methodology outlined by Brunken et al. (2024), where they demonstrated the necessity of including warm and hot ice species in the fitting process for HOPS 370. Specifically, we utilized laboratory spectra of pure CO_2 at 80 K, $\text{CO}_2\text{:H}_2\text{O}$ (1:10) at 160 K, and $\text{CO}_2\text{:CH}_3\text{OH}$ (3:1) at 105 K, obtained from the Leiden Ice Database for Astrochemistry (LIDA)¹ (Rocha et al.

2022), to model the observed $^{13}\text{CO}_2$ absorption feature at $4.38 \mu\text{m}$ (Figure 8[a] and 8[b]).

Due to the feature overlap, the decomposition of OCN^- and CO ice was done simultaneously (Figure 8[c] and 8[d]). We used a mixture of Gaussian and Lorentzian functions to fit the absorption feature (see for details Pontoppidan et al. 2003; van Broekhuizen et al. 2005; Boogert et al. 2022, and references therein). Components for both the OCN^- and CO are described in Table 1. See Nazari et al. 2024 for details about OCN^- ice.

Figures 8[a] and 8[c] show the peak optical depth maps of various fitted components of $^{13}\text{CO}_2$, OCN^- , and CO . Both figures demonstrate an excess of polar species relative to apolar species across the entire FOV. The dom-

¹ <https://icedb.strw.leidenuniv.nl/>

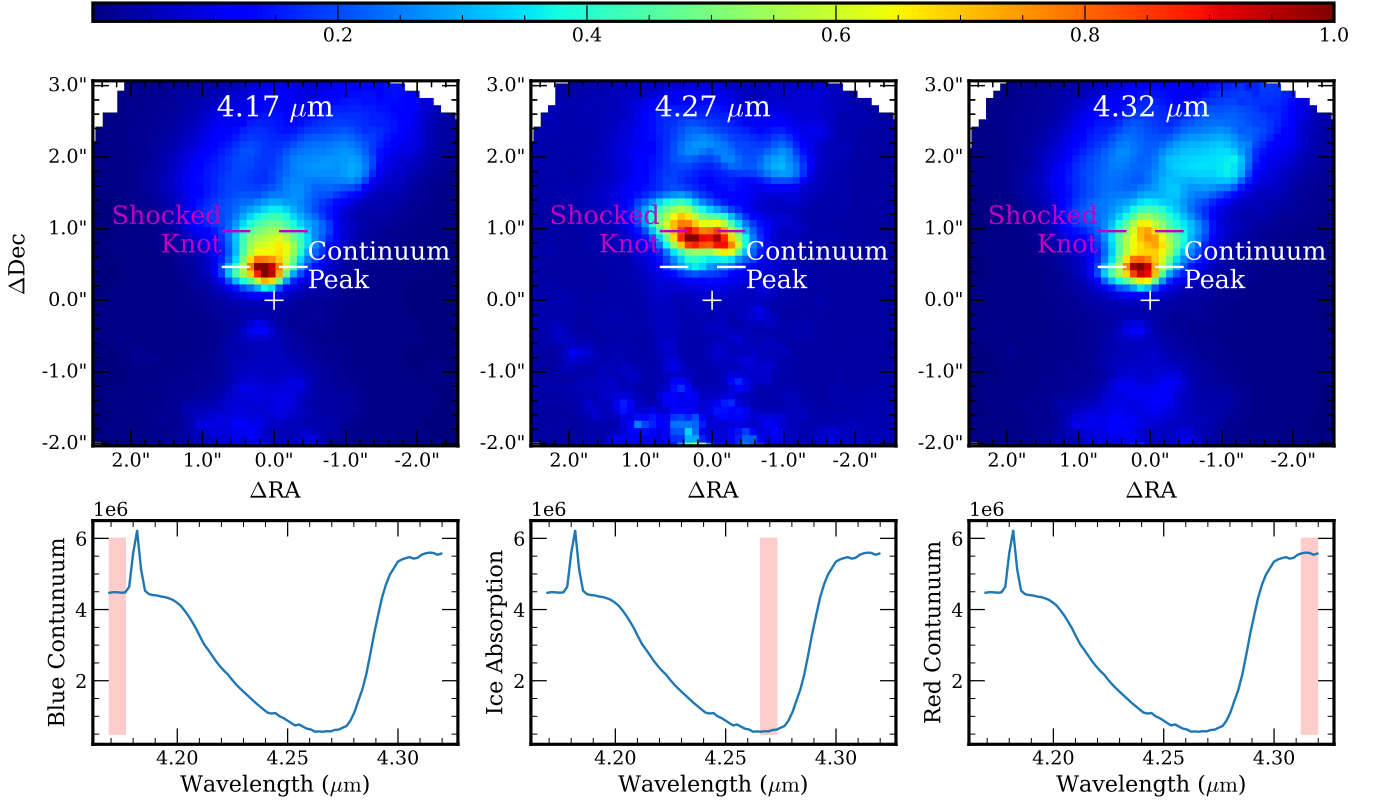


Figure 6. *Top:* Normalized mean channel maps from NIRSPEC observations showing the differences in observed intensities between the continuum and CO₂ ice absorption wavelengths. The mean wavelength corresponding to each map is indicated at the top of each panel. *Bottom:* The red-shaded regions in the spectra below each map highlight the spectral range used to create the mean channel maps. The white ‘+’ symbol denotes the position of the ALMA continuum. *Note:* The source [MGM2012] 2301 is masked in this figure.

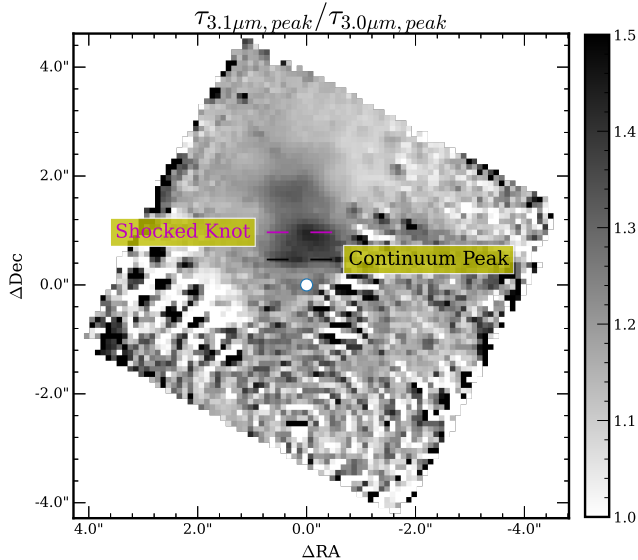


Figure 7. Ratio of peak optical depth map of H₂O at 3.1 μm (crystalline H₂O) to peak optical depth map of H₂O at 3.0 μm (amorphous H₂O). The white circle marks the ALMA continuum position.

Table 1. CO and OCN⁻ Component Profiles

Component	Profile	Center (μm)	FWHM (μm)
Apolar OCN ⁻	Gaussian	4.5969	0.0317
Polar OCN ⁻	Gaussian	4.6174	0.0554
Blue CO	Gaussian	4.6648	0.0065
Apolar CO	Gaussian	4.6731	0.0076
Polar CO	Lorentzian	4.6806	0.0232

inance of the polar CO component relative to the apolar CO component across FOV and the requirement of hot/warm ice components to fit the ¹³CO₂ absorption profile suggests thermal processing throughout the envelope (see Section 4.1). The maps also show a minimum in the optical depth coincident with the bright knot in the H₂ 0-0 located ~ 1'' north of the ALMA continuum position.

4. DISCUSSION

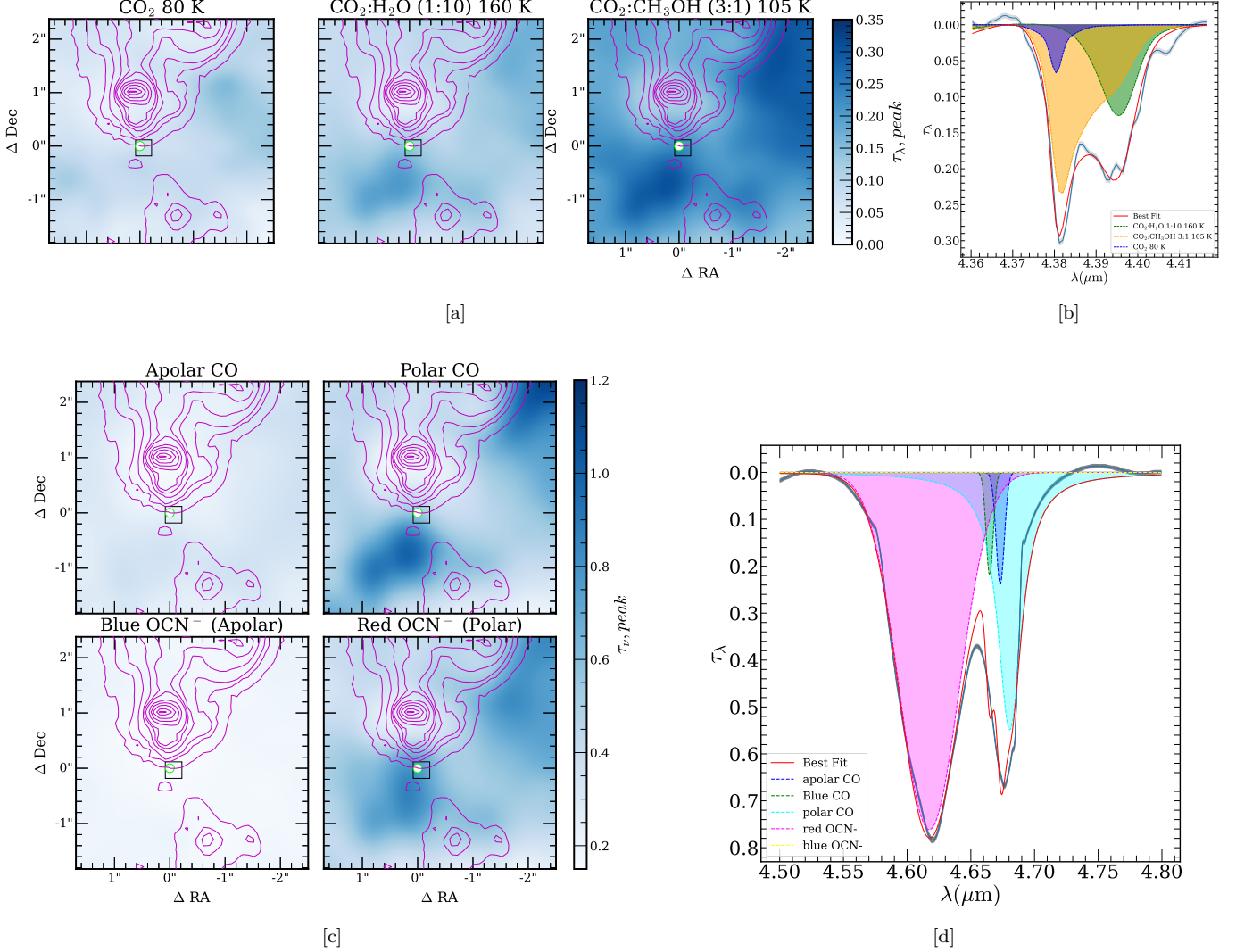


Figure 8. [a]: Decomposed maps of $^{13}\text{CO}_2$. The figure shows three components from left to right: CO_2 at 80 K, $\text{CO}_2:\text{H}_2\text{O}$ (1:10) at 160 K, and $\text{CO}_2:\text{CH}_3\text{OH}$ (3:1) 105 K. All panels use colormaps to represent the peak optical depth. A lime circle marks the ALMA continuum position, and the magenta color contour overlaid displays the H_2 0 – 0 S(11) emission in the FOV. The contour levels are 0.015, 0.03, 0.05, 0.1, 0.15, 0.2, 0.35, 0.5, 0.67, 0.85, $0.97 \times$ (Maximum of H_2 0 – 0 S(11) emission). The densest contours ($1''$ north to the ALMA continuum) mark the shocked knot. [b]: A fitting example of decomposition of $^{13}\text{CO}_2$ ice for the black cell marked in the peak optical depth maps in [a].

[c]: Decomposed maps of CO and OCN^- ice. The *top* row displays the apolar (left) and polar (right) components of CO, while the bottom row shows the apolar (left) and polar (right) components of OCN^- . All panels use colormaps to represent the peak optical depth. The overlaid lime circle and magenta color contours are similar to those on the panel [a]. [d]: A fitting example of decomposition of CO and OCN^- ice features for the black cell marked in the peak optical depth maps in [c].

The energetic processes in the protostellar phase, such as protostellar irradiation, episodic accretion-drive outbursts, and shocks driven by jets/outflows, can potentially change the chemical composition or the physical structure of the envelope material. Direct observation of these phenomena in action has been previously limited due to lack of sensitivity and angular resolution. However, the unique combination of JWST NIR-

Spec+MIRI’s sensitivity, angular resolution, and broad spectral coverage ($2.8 \mu\text{m}$ to $28 \mu\text{m}$) has finally made these detailed studies feasible.

Our latest observations of HOPS 370 using JWST NIRSpec and MIRI reveal the chemical inventory and previously unseen details of the ice distribution within the envelope. In this section, we discuss the results obtained in the Section 3.

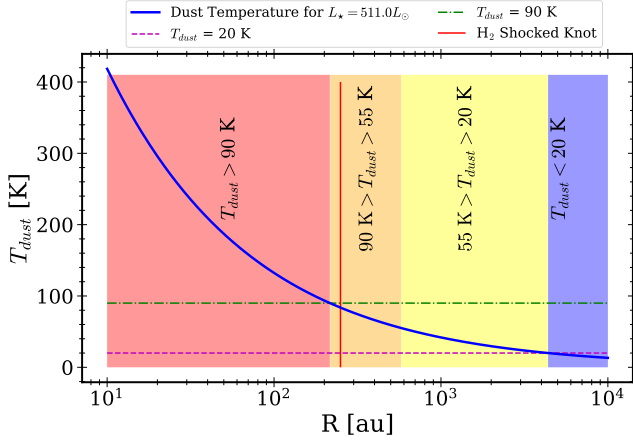


Figure 9. Radial profile of dust temperature of the HOPS 370 envelope. The color-shaded regions mark various dust temperature zones. The red vertical line represents the inclination corrected distance of the H₂ shocked knot from the central protostar.

4.1. Warm Envelope

As demonstrated in Section 3, multiple ice absorption signatures (e.g., weak CO ice, double-peaked 4.38 μm CO₂, double-peaked 15.2 μm CO₂, and the presence of crystalline water) provide evidence for significant envelope heating in HOPS 370 (Pontoppidan et al. 2008; Boogert et al. 2015; Kim et al. 2022; Brunken et al. 2024). Some of these signatures, e.g., double-peaked ¹³CO₂ ice features are quite extended (see Figure 3). Additionally, CO ice absorption is much weaker relative to CO₂ everywhere in the envelope (see Figures 4 and 5). All of these together suggest thermal processing of ice species throughout the envelope in our FOV.

Additionally, the decomposed maps of CO, and OCN⁻ (see Figure 8[c]) show that the polar mixtures of these ice species have higher optical depths across the envelope relative to the apolar mixtures. The sublimation temperatures of polar mixtures are relatively higher than those of apolar mixtures (e.g., the sublimation temperatures of polar CO and apolar CO are ~ 90 K and ~ 20 K, respectively, see also Boogert et al. 2015). The combination of weak CO ice absorption, dominated by the polar mixture, along with the presence of strong rovibrational CO lines in emission (see Figure 3), strongly suggest the possibility of CO ice sublimation in the inner envelope up to ~ 800 au (the extent of the decomposed maps) from the central protostar.

To explore the potential cause of the thermal processing of ice species over this spatial extent, we calculate the radial profile of the dust temperature in the envelope. For simplicity, we assume the envelope to be spherical and compute the equilibrium temperature of a dust

grain at a distance R from the central protostar. Assuming dust grains to be perfect blackbodies, the temperature of the dust grain (T_{dust}) at a distance R from the protostar with luminosity L_* is given by:

$$T_{dust}(R) = \left[\frac{L_*}{16\pi\sigma R^2} \right]^{1/4} \quad (2)$$

Figure 9 shows the radial profile of dust temperature. A total luminosity of 511 L_\odot was used for this calculation (Furlan et al. 2016; Tobin et al. 2020b). The radial profile of dust temperature shows that dust may have temperatures above 20 K and 90 K for radial distances less than ~ 4000 and ~ 200 au, respectively. These temperatures are high enough to explain the extended ice heating observed in HOPS 370’s envelope. Hence, the envelope heating to this spatial extent in HOPS 370 can likely be attributed to its high total luminosity, 511 L_\odot , due to the large accretion rate of $\dot{M}_{acc} \sim 2.25 \times 10^{-5} M_\odot \text{yr}^{-1}$ (Tobin et al. 2020b). However, the exact mechanism responsible for the high accretion rate in HOPS 370, whether it is in a steady state or in a burst phase, is still a matter of debate (Tobin et al. 2020b). Nevertheless, given the simplistic assumptions made in the calculations, a detailed radiative transfer modeling study is required to understand the details of the thermal structure of the envelope in the future.

4.2. Is there a Local Ice Deficit in the Inner Envelope?

Instead of a smooth decrement in the envelope dust density as a function of distance from the central protostar, the peak optical depth maps of volatiles such as H₂O, CO₂, ¹³CO₂, CO, and OCN⁻ reveal a highly structured spatial distribution of ice species column density in the envelope (see Figures 4 and 5). Further, channel maps in Figure 6 show a remarkable difference in the observed intensity distribution at peak ice absorption wavelengths compared to ice absorption-free/continuum wavelengths. The normalized channel maps show that, at peak ice absorption wavelengths, not all background scattered light is absorbed by the ices in the envelope. The scattered light leaks through an elliptical patch, spatially overlapping with the H₂ and OH shocked knots. These signatures suggest relatively less absorption of light by ice species at the shocked knot position. There is another low opacity bar-like region northwest of the shocked knot position ($\sim 2''$ north of the ALMA continuum position).

To confirm the lack of absorption offered by ice species at these low-opacity regions, we generated extinction (A_V) and column density maps using the CO₂ ice absorption band. To produce a column density map of

CO₂, we use the following equation at each spaxel,

$$N_{CO_2} = \frac{1}{A} \int \tau_\nu d\nu \quad (3)$$

where $A = 1.1 \times 10^{-16} \text{ cm mol}^{-1}$ is the density-corrected band strength (Gerakines et al. 1995; Bouilloud et al. 2015). Next, we generate the extinction map using the KP5 extinction law (Pontoppidan et al. 2024).

We used the relation $A_\lambda = 2.5 \log(e) N \kappa_{\text{ext}}(\lambda)$, where $\kappa_{\text{ext}}(\lambda)$ and N represent the mass absorption coefficient and mass column density, respectively (Pontoppidan et al. 2024). Then,

$$\frac{A_V}{A_\lambda} = \frac{\kappa_{\text{ext}}(V)}{\kappa_{\text{ext}}(\lambda)} \quad (4)$$

At each spaxel, we used the optical depth (τ_λ) at $4.27 \mu\text{m}$ of CO₂ ice absorption feature to calculate A_λ . Using equation 4, we were able to calculate A_V at each spaxel. We present the extinction and column density maps obtained using the $4.27 \mu\text{m}$ CO₂ feature in the left and middle panels of Figure 10, respectively. The shocked knot marked by magenta-colored lines coincides with the lower extinction and lower column density regions.

We independently measure the extinction values towards the shocked knot using H₂ 0-0 S(*J*) rotational lines (for details, see Narang et al. 2024; Neufeld et al. 2024; Tyagi et al. in prep.), which provides a measure of extinction independent of ice optical depth. Four circular apertures of radius $0.4''$ —labeled as 0, 1, 2, and 3 are depicted in black, magenta, red, and orange, respectively in the middle panel of Figure 10 – were used to calculate A_V . We find that aperture 1, which spatially coincides with the low optical depth region and the shocked knot, exhibits a lower A_V value by ~ 2 magnitude compared to aperture 0 and 2 (see dot markers in the right panel of Figure 10). Similarly, aperture 3 has a lower extinction than aperture 0, and 2 has a higher extinction than aperture 1. The H₂ rotational diagrams at apertures 0, 1, 2, and 3 are presented in Appendix B.

In the same panel, we have marked the mean A_V values of these apertures calculated using the CO₂ ice with a cross marker for comparison. Both measurements exhibit a similar trend; however, the A_V values obtained from CO₂ ice are consistently higher than those obtained from the H₂ analysis. The difference may come from differences between the actual and adopted extinction law. Alternatively, a weak component of foreground H₂ may also lower the extinction in this band.

Despite the difference in the absolute extinction values, this test independently verifies that indeed there is a lack of column density of material at the shocked knot

position and the Br α fish-hook-like structure. We call this low optical depth region around the shocked knot an *extinction minimum* in the envelope of HOPS 370. In Appendix C, we further explore the effects of scattered light on the optical depth of CO₂ absorption feature.

Below, we explore the possible explanations for the observed substructures in the envelope ice density.

4.2.1. Can Intense UV Radiation from the Strong Shocked Knot Produce Localized Excess Heating?

The bright knot in the outflow, apparent in the H₂ and Br α maps, spatially coincides with the ice column density deficiency structure of the envelope. We also observe increased relative crystallization of H₂O at the shocked knot position (see Figure 7) suggesting excess heating at the shocked knot position (marked by magenta lines in all the Figures). Neufeld et al. 2024 have reported a suprathreshold OH emission that peaks at the same knot position and attributed the suprathreshold OH emission to the photodissociation of water by UV photons. Furthermore, the second ice deficit column density structure (roughly $2''$ north of the ALMA continuum position) also spatially coincides with the fish-hook-like structure of Br α emission (see third panel of Figure 1), again demonstrating the presence of UV photons at the ice deficit position. These findings, taken together, suggest that UV photons originating from the shocked emission in jets/outflows could be responsible for excess heating of the inner envelope wall. This heating likely leads to the ice deficit through the sublimation of icy grain mantles and enhances the relative crystallization of H₂O ice.

However in such a scenario, if we assume the shocked knot is located on the collimated jet axis, one would expect more uniform heating of the envelope instead of the heating concentrated in a localized region. Further, the low optical depth regions show low A_V values calculated using H₂ lines suggesting low total (ice+dust) column densities in these regions (see Figure 10). For this hypothesis to hold true, UV photons originating from the shocked knot would need also to destroy/sublimate dust. However, given the high sublimation temperature of silicate dust grains ($\sim 1500 \text{ K}$) and the fact that only a small fraction of UV photons escape the shocked knot region (Neufeld et al. 2024), this scenario is less likely to explain our observations.

4.2.2. Variable Extinction due to Foreground Material or Initial Conditions

The localized ice deficit and variable extinction observed in HOPS 370 (see Figures 4 and 5) could be attributed to the initial conditions and collapse mecha-

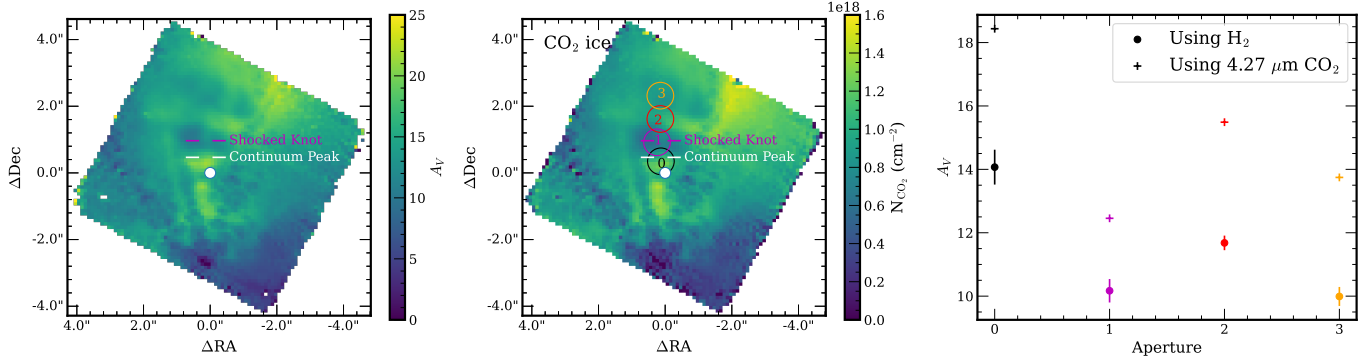


Figure 10. Extinction and column density maps using the $4.27 \mu\text{m CO}_2$ feature. The *left* panel shows the visual extinction (A_V) map using KP5 and the peak optical depth of the CO_2 feature. The *middle* panel shows the column density map of CO_2 , derived using the band strength of CO_2 at $4.27 \mu\text{m}$. The shocked knot peak of H_2 and the continuum peak are marked by magenta and white color lines, respectively. The white-filled circle marks the ALMA continuum position. Black, magenta, red, and orange circles, marked by numbers 0, 1, 2, and 3 are the apertures used to calculate the extinction independently using H_2 rotational lines. The *right* panel shows the measured extinction (A_V) corresponding to the apertures marked in the middle panel using H_2 rotational lines and $4.27 \mu\text{m CO}_2$ feature in cross and dot markers, respectively.

nism of its envelope, or possibly to variable foreground extinction.

A simple case of variable foreground extinction of the molecular cloud could in principle also explain our observations. However, the protostellar envelope is the densest part along our line of sight and column density is lower by a factor of ~ 2 at the shocked knot (see Figure 10). Given these facts, this scenario is unlikely to explain our observations.

In the case of initial conditions, we assume that the initial core density has density irregularities and asymmetries. Then, the structures in the envelope column density might arise due to a rapid turbulent collapse of the envelope which did not give enough damping time to smooth out the initial density irregularities (see also Tobin et al. 2010). In this scenario, the density deficit could be concentrated in specific regions, such as the inner cavity wall and the envelope’s outer edge, or it could potentially exist throughout the envelope along our line of sight. Additionally, this case suggests an irregular supply of envelope material to the protostellar disk, which may affect episodic accretion due to disk instability. In this case, these regions would represent the initial “seeds” that might originate the gravitational instabilities at the base of accretion bursts.

Assuming that the density deficit occurs in the colder part of the envelope, the relatively high crystallization of H_2O ice at the shocked knot can be explained. In this scenario, our observations would probe the inner heated regions of the envelope, while the line of sight would be depleted of the colder material in the outer parts of the envelope. This absence of colder material would manifest as localized excess heating within the envelope.

Figure 11 displays a simplified cartoon depicting such a scenario.

5. CONCLUSION

Our JWST NIRSpec IFU and MIRI MRS observations of the intermediate-mass protostar HOPS 370 (OMC2-FIR3) demonstrate that during the protostellar phase the envelope can be significantly heated, thereby providing conditions for further processing of building material for the protostellar/protoplanetary disk. This study presents a rich inventory of gas-phase and ice-phase species in the spectral range from $2.8 \mu\text{m}$ to $28 \mu\text{m}$. Further, we present the first high spatial resolution (~ 80 au) maps of ice species in the protostellar envelope using NIRSpec data. Below we summarize our key findings from these observations:

1. The envelope of HOPS 370 exhibits clear evidence of thermally processed ices, seen in various ice absorption features: crystalline H_2O , double-peaked $^{13}\text{CO}_2$, and the double-peaked $15.2 \mu\text{m CO}_2$.
2. The decomposed maps of CO and OCN^- show that the polar mixture of ice species dominates the entire inner envelope, indicating additional evidence for thermal processing. Weak CO ice absorption compared to CO_2 together with strong CO ro-vibrational gas phase lines further suggest CO ice sublimation in the envelope.
3. Optical depth and column density maps of volatile ice species reveal a nonuniform and structured density distribution of the protostellar envelope with a minimum in ice column density and line-of-sight extinction coincident with a prominent shock heated knot in an outflow jet.

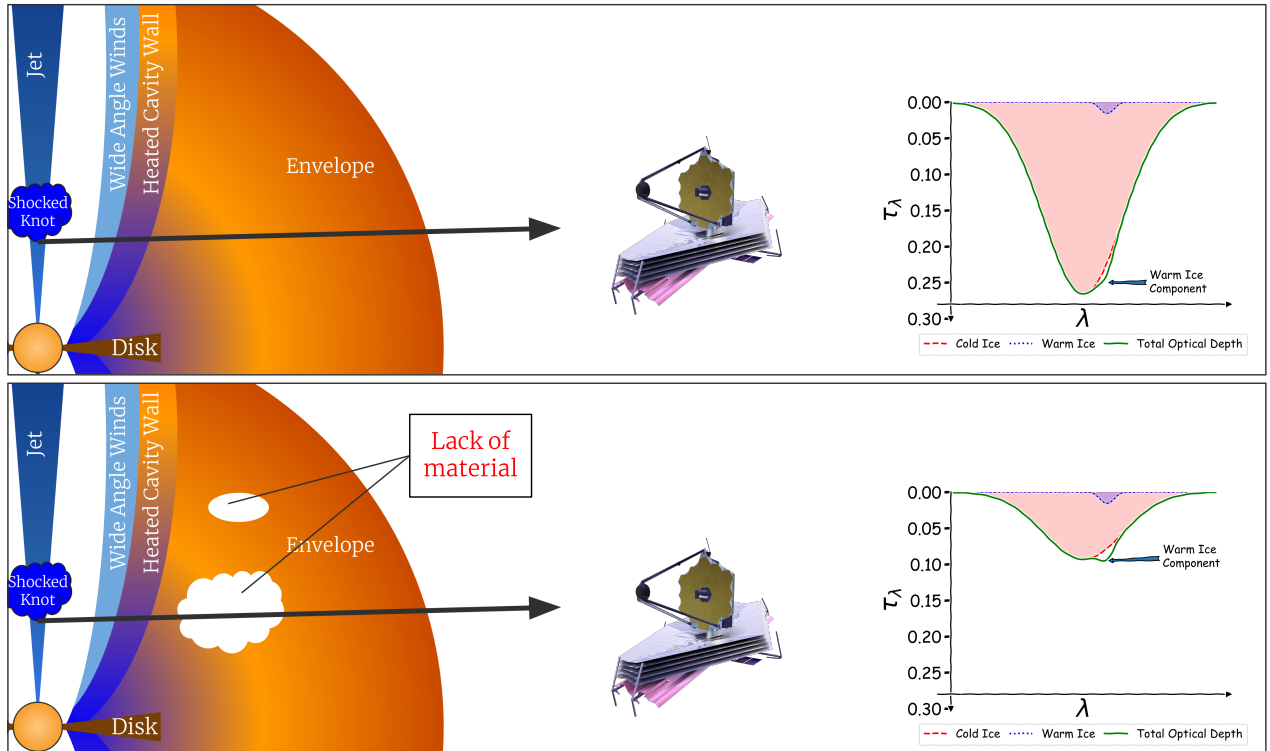


Figure 11. A simple cartoon diagram depicting the difference between theoretical (top panel) vs observed/proposed (bottom panel) density structure of the protostellar envelope. Cartoon models of the optical depth of an ice feature consisting of warm and cold ice are also shown for both cases. In the ice cartoon models, the green line shows the observed absorption profile by the JWST while the blue dotted line and green dashed lines represent the warm and cold ice components. *The image is not to scale.*

4. Dust extinction measured with H_2 rotational lines show a region of lower extinction, and hence lower dust column density region, at the shocked knot position.
5. The enhanced relative crystallization of H_2O observed around the shocked knot position suggests local excess heating or deficit of outer colder envelope material along the line of sight.
6. We propose that the irregular structure in the envelope has resulted in a lower column density/extinction line of sight, and the observed emission along this sightline is dominated by the inner thermally processed ices near the outflow cavity wall. This shows clear evidence of the thermal processing of the ice closer to the inner cavity wall. The spatial coincidence of the shocked knot seen in H_2 and $\text{Br}\alpha$ emission along this line of sight appears to be a chance alignment.

Although the high luminosity of HOPS 370 dominates the envelope heating, the role and contribution of the outflow shocks in thermal processing of the protostellar envelope have not been fully explored yet. Future

observations of low-luminosity protostars (where protostellar luminosity is inefficient in heating the envelope) with JWST may reveal the role of outflow shocks in the thermal processing of ices in the envelope.

6. DATA AVAILABILITY

All of the data presented in this article were obtained from the Mikulski Archive for Space Telescopes (MAST) at the Space Telescope Science Institute. The specific observations analyzed can be accessed via DOI: [10.17909/3kky-t040](https://doi.org/10.17909/3kky-t040).

7. ACKNOWLEDGMENT

This work is based on observations made with the NASA/ESA/CSA James Webb Space Telescope. The data were obtained from the Mikulski Archive for Space Telescopes at the Space Telescope Science Institute, which is operated by the Association of Universities for Research in Astronomy, Inc., under NASA contract NAS 5-03127 for JWST. These observations are associated with program #1802. H.T. and P.M. acknowledge the support of the Department of Atomic Energy, Government of India, under Project Identification No. RTI 4002. Support for SF, AER, STM,

RG, WF, JG, JJT, and DW in program #1802 was provided by NASA through a grant from the Space Telescope Science Institute, which is operated by the Association of Universities for Research in Astronomy, Inc., under NASA contract NAS 5-03127. D.A.N. was supported by grant SOF08-0038 from USRA. A.C.G. has been supported by PRIN-MUR 2022 20228JPA3A “The path to star and planet formation in the JWST era (PATH)” and by INAF-GoG 2022 “NIR-dark Accretion Outbursts in Massive Young stellar objects (NAOMY)”. G.A. and M.O., acknowledge financial support from grants PID2020-114461GB-I00 and CEX2021-001131-S, funded by MCIN/AEI/10.13039/501100011033. Y.-L.Y. acknowledges support from Grant-in-Aid from the Ministry of Education, Culture, Sports, Science, and

Technology of Japan (20H05845, 20H05844, 22K20389), and a pioneering project in RIKEN (Evolution of Matter in the Universe). Leiden astrochemistry thanks support from the European Research Council (ERC) under the European Union’s Horizon 2020 research and innovation programme (grant agreement No. 101019751 MOLDISK). AS gratefully acknowledges support by the Fondcyt Regular (project code 1220610), and ANID BASAL project FB210003.

Facility: JWST (NIRSpec, MIRI)

Software: Astropy (Astropy Collaboration et al. 2013, 2018, 2022); CARTA (Comrie et al. 2021); Matplotlib (Hunter 2007); NumPy (Harris et al. 2020); SciPy (Virtanen et al. 2020).

REFERENCES

- ALMA Partnership, Brogan, C. L., Pérez, L. M., et al. 2015, *ApJL*, 808, L3
- Altwegg, K., Balsiger, H., & Fuselier, S. A. 2019, *ARA&A*, 57, 113
- Arce, H. G., Santiago-García, J., Jørgensen, J. K., Tafalla, M., & Bachiller, R. 2008, *ApJL*, 681, L21
- Armitage, P. J. 2020, *Astrophysics of planet formation*, Second Edition
- Astropy Collaboration, Price-Whelan, A. M., Lim, P. L., et al. 2022, *ApJ*, 935, 167
- Astropy Collaboration, Price-Whelan, A. M., Sipőcz, B. M., et al. 2018, *AJ*, 156, 123
- Astropy Collaboration, Robitaille, T. P., Tollerud, E. J., et al. 2013, *A&A*, 558, A33
- Beuther, H., van Dishoeck, E. F., Tychoniec, L., et al. 2023, *A&A*, 673, A121
- Böker, T., Arribas, S., Lützgendorf, N., et al. 2022, *A&A*, 661, A82
- Boogert, A. C. A., Brewer, K., Brittain, A., & Emerson, K. S. 2022, *ApJ*, 941, 32
- Boogert, A. C. A., Ehrenfreund, P., Gerakines, P. A., et al. 2000, *A&A*, 353, 349
- Boogert, A. C. A., Gerakines, P. A., & Whittet, D. C. B. 2015, *ARA&A*, 53, 541
- Bouilloud, M., Fray, N., Bénilan, Y., et al. 2015, *MNRAS*, 451, 2145
- Brownlee, D., Tsou, P., Aléon, J., et al. 2006, *Science*, 314, 1711
- Brunken, N. G. C., Rocha, W. R. M., van Dishoeck, E. F., et al. 2024, *arXiv e-prints*, arXiv:2402.04314
- Ciesla, F. J. 2010, *Icarus*, 208, 455
- Cleeves, L. I., Bergin, E. A., Alexander, C. M. O. D., et al. 2014, *Science*, 345, 1590
- Codella, C., Fontani, F., Ceccarelli, C., et al. 2015, *MNRAS*, 449, L11
- Comrie, A., Wang, K.-S., Hsu, S.-C., et al. 2021, CARTA: The Cube Analysis and Rendering Tool for Astronomy
- Dartois, E., Noble, J. A., Caselli, P., et al. 2024, *Nature Astronomy*, 8, 359
- Dartois, E., Noble, J. A., Ysard, N., Demyk, K., & Chabot, M. 2022, *A&A*, 666, A153
- Drozdovskaya, M. N., van Dishoeck, E. F., Rubin, M., Jørgensen, J. K., & Altwegg, K. 2019, *MNRAS*, 490, 50
- Ehrenfreund, P., Boogert, A. C. A., Gerakines, P. A., Tielens, A. G. G. M., & van Dishoeck, E. F. 1997, *A&A*, 328, 649
- Federman, S., Megeath, S. T., Tobin, J. J., et al. 2023, *ApJ*, 944, 49
- Federman, S. A., Megeath, S. T., Rubinstein, A. E., et al. 2024, *ApJ*, 966, 41
- Fischer, W. J., Megeath, S. T., Furlan, E., et al. 2017, *ApJ*, 840, 69
- Francis, L., van Gelder, M. L., van Dishoeck, E. F., et al. 2024, *A&A*, 683, A249
- Furlan, E., Fischer, W. J., Ali, B., et al. 2016, *ApJS*, 224, 5
- Gerakines, P. A., Schutte, W. A., Greenberg, J. M., & van Dishoeck, E. F. 1995, *A&A*, 296, 810
- González-García, B., Manoj, P., Watson, D. M., et al. 2016, *A&A*, 596, A26
- Gordon, I. E., Rothman, L. S., Hargreaves, R. J., et al. 2022, *JQSRT*, 277, 107949
- Harris, C. R., Millman, K. J., van der Walt, S. J., et al. 2020, *Nature*, 585, 357
- Hartmann, L. 2009, *Accretion Processes in Star Formation: Second Edition*

- Hartogh, P., Lis, D. C., Bockelée-Morvan, D., et al. 2011, *Nature*, 478, 218
- Hunter, J. D. 2007, *Computing in Science & Engineering*, 9, 90
- Jakobsen, P., Ferruit, P., Alves de Oliveira, C., et al. 2022, *A&A*, 661, A80
- Jones, O. C., Álvarez-Márquez, J., Sloan, G. C., et al. 2023, *MNRAS*, 523, 2519
- Jørgensen, J. K., Belloche, A., & Garrod, R. T. 2020, *ARA&A*, 58, 727
- Kim, H. J., Evans, Neal J., I., Dunham, M. M., Lee, J.-E., & Pontoppidan, K. M. 2012, *ApJ*, 758, 38
- Kim, J., Lee, J.-E., Jeong, W.-S., et al. 2022, *ApJ*, 935, 137
- Kramida, A. & Ralchenko, Y. 1999, NIST Atomic Spectra Database, NIST Standard Reference Database 78
- Lefloch, B., Ceccarelli, C., Codella, C., et al. 2017, *MNRAS*, 469, L73
- Manara, C. F., Morbidelli, A., & Guillot, T. 2018, *A&A*, 618, L3
- McClure, M. K., Rocha, W. R. M., Pontoppidan, K. M., et al. 2023, *Nature Astronomy*, 7, 431
- Megeath, S. T., Gutermuth, R., Muzerolle, J., et al. 2012, *AJ*, 144, 192
- Megeath, T., Anglada, G., Atnagulov, P., et al. 2021, Investigating Protostellar Accretion Across the Mass Spectrum, JWST Proposal. Cycle 1, ID. #1802
- Morbidelli, A., Lunine, J. I., O'Brien, D. P., Raymond, S. N., & Walsh, K. J. 2012, *Annual Review of Earth and Planetary Sciences*, 40, 251
- Mumma, M. J. & Charnley, S. B. 2011, *ARA&A*, 49, 471
- Narang, M., Manoj, P., Tyagi, H., et al. 2023, *Journal of Astrophysics and Astronomy*, 44, 92
- Narang, M., Manoj, P., Tyagi, H., et al. 2024, *ApJL*, 962, L16
- Nazari, P., Rocha, W. R. M., Rubinstein, A. E., et al. 2024, *arXiv e-prints*, arXiv:2401.07901
- Neufeld, D. A., Manoj, P., Tyagi, H., et al. 2024, *ApJL*, 966, L22
- Öberg, K. I. & Bergin, E. A. 2021, *PhR*, 893, 1
- Ohashi, N., Tobin, J. J., Jørgensen, J. K., et al. 2023, *ApJ*, 951, 8
- Osorio, M., Díaz-Rodríguez, A. K., Anglada, G., et al. 2017, *ApJ*, 840, 36
- Pontoppidan, K. M., Boogert, A. C. A., Fraser, H. J., et al. 2008, *ApJ*, 678, 1005
- Pontoppidan, K. M., Evans, II, N., Bergner, J., & Yang, Y.-L. 2024, *Res. Notes AAS*, 8, 68
- Pontoppidan, K. M., Fraser, H. J., Dartois, E., et al. 2003, *A&A*, 408, 981
- Pontoppidan, K. M., Salyk, C., Bergin, E. A., et al. 2014, in *Protostars and Planets VI*, ed. H. Beuther, R. S. Klessen, C. P. Dullemond, & T. Henning, 363–385
- Rieke, G. H., Wright, G. S., Böker, T., et al. 2015, *PASP*, 127, 584
- Rocha, W. R. M., Rachid, M. G., Olsthoorn, B., et al. 2022, *A&A*, 668, A63
- Rocha, W. R. M., van Dishoeck, E. F., Ressler, M. E., et al. 2024, *A&A*, 683, A124
- Rubin, M., Altwegg, K., Balsiger, H., et al. 2018, *Science Advances*, 4, eaar6297
- Rubinstein, A. E., Tyagi, H., Nazari, P., et al. 2023, *arXiv e-prints*, arXiv:2312.07807
- Segura-Cox, D. M., Schmiedeke, A., Pineda, J. E., et al. 2020, *Nature*, 586, 228
- Sheehan, P. D. & Eisner, J. A. 2018, *ApJ*, 857, 18
- Sheehan, P. D., Tobin, J. J., Federman, S., Megeath, S. T., & Looney, L. W. 2020, *ApJ*, 902, 141
- Slavicinska, K., van Dishoeck, E. F., Tychoniec, L., et al. 2024, *arXiv e-prints*, arXiv:2404.15399
- Stahler, S. W. & Palla, F. 2004, *The Formation of Stars*
- Sturm, J. A., McClure, M. K., Beck, T. L., et al. 2023, *A&A*, 679, A138
- Takahashi, S., Saito, M., Ohashi, N., et al. 2008, *ApJ*, 688, 344
- Tanaka, Y. A. & Tsukamoto, Y. 2019, *MNRAS*, 484, 1574
- Taquet, V., Wirstrom, E. S., & Charnley, S. B. 2016, *ApJ*, 821, 46
- Terebey, S., Shu, F. H., & Cassen, P. 1984, *ApJ*, 286, 529
- Tobin, J. J., Hartmann, L., Looney, L. W., & Chiang, H.-F. 2010, *ApJ*, 712, 1010
- Tobin, J. J. & Sheehan, P. D. 2024, *arXiv e-prints*, arXiv:2403.15550
- Tobin, J. J., Sheehan, P. D., Megeath, S. T., et al. 2020a, *ApJ*, 890, 130
- Tobin, J. J., Sheehan, P. D., Reynolds, N., et al. 2020b, *ApJ*, 905, 162
- Tsukamoto, Y., Okuzumi, S., & Kataoka, A. 2017, *ApJ*, 838, 151
- Tychoniec, L., Manara, C. F., Rosotti, G. P., et al. 2020, *A&A*, 640, A19
- Tychoniec, L., van Gelder, M. L., van Dishoeck, E. F., et al. 2024, *arXiv e-prints*, arXiv:2402.04343
- van Broekhuizen, F. A., Pontoppidan, K. M., Fraser, H. J., & van Dishoeck, E. F. 2005, *A&A*, 441, 249
- van Dishoeck, E. F., Bergin, E. A., Lis, D. C., & Lunine, J. I. 2014, in *Protostars and Planets VI*, ed. H. Beuther, R. S. Klessen, C. P. Dullemond, & T. Henning, 835–858
- Virtanen, P., Gommers, R., Oliphant, T. E., et al. 2020, *Nature Methods*, 17, 261

Visser, R., Bergin, E. A., & Jørgensen, J. K. 2015, *A&A*,
577, A102

Visser, R., van Dishoeck, E. F., Doty, S. D., & Dullemond,
C. P. 2009, *A&A*, 495, 881

Wright, G. S., Wright, D., Goodson, G. B., et al. 2015,
PASP, 127, 595

Yang, Y.-L., Green, J. D., Pontoppidan, K. M., et al. 2022,
ApJL, 941, L13

APPENDIX

A. LINE LIST

Table A1. Detected Molecular lines. Molecular line information is taken from HITRAN (Gordon et al. 2022).

Species	Wavelength (μm)	Transition, v	Transition, J
OH	2.9343	X3/2 1 – X3/2 0	PP 4.5ee
OH	2.9346	X3/2 1 – X3/2 0	PP 4.5ff
OH	2.9603	X1/2 1 – X1/2 0	PP 4.5ff
OH	2.9604	X1/2 1 – X1/2 0	PP 4.5ee
OH	2.9700	X3/2 1 – X3/2 0	PP 5.5ee
OH	2.9704	X3/2 1 – X3/2 0	PP 5.5ff
OH	3.0415	X1/2 1 – X1/2 0	PP 6.5ff
OH	3.0418	X1/2 1 – X1/2 0	PP 6.5ee
OH	3.0481	X3/2 1 – X3/2 0	PP 7.5ee
OH	3.0487	X3/2 1 – X3/2 0	PP 7.5ff
OH	3.0850	X1/2 1 – X1/2 0	PP 7.5ff
OH	3.0855	X1/2 1 – X1/2 0	PP 7.5ee
OH	3.0906	X3/2 1 – X3/2 0	PP 8.5ee
OH	3.0913	X3/2 1 – X3/2 0	PP 8.5ff
OH	3.1354	X3/2 1 – X3/2 0	PP 9.5ee
OH	3.1363	X3/2 1 – X3/2 0	PP 9.5ff
H ₂	5.0530	0 – 0	S(8)
H ₂	5.5116	0 – 0	S(7)
H ₂	5.8112	1 – 1	S(7)
H ₂ O	5.8608	010 – 000	2 2 0 – 1 1 1
H ₂ O	5.8830	010 – 000	2 2 1 – 1 1 0
H ₂ O	5.8967	010 – 000	5 0 5 – 4 1 4
H ₂ O	5.9356	010 – 000	4 1 4 – 3 0 3
H ₂ O	5.9701	010 – 000	4 0 4 – 3 1 3
H ₂ O	5.9904	010 – 000	3 1 3 – 2 0 2
H ₂ O	6.0142	010 – 000	2 2 1 – 2 1 2
H ₂ O	6.0490	010 – 000	2 1 2 – 1 0 1
H ₂ O	6.0521	010 – 000	3 0 3 – 2 1 2
H ₂ O	6.0670	010 – 000	2 2 0 – 2 1 1
H ₂ O	6.0757	010 – 000	3 2 1 – 3 1 2
H ₂	6.1088	0 – 0	S(6)
H ₂ O	6.1140	010 – 000	3 1 2 – 3 0 3
H ₂ O	6.1166	010 – 000	1 1 1 – 0 0 0

Table A1 *continued*

Table A1 (*continued*)

Species	Wavelength (μm)	Transition, v	Transition, J
H ₂ O	6.1434	010 - 000	2 0 2 - 1 1 1
H ₂ O	6.1596	010 - 000	2 1 1 - 2 0 2
H ₂ O	6.1857	010 - 000	1 1 0 - 1 0 1
H ₂ O	6.3447	010 - 000	1 0 1 - 1 1 0
H ₂ O	6.3705	010 - 000	2 0 2 - 2 1 1
H ₂ O	6.3740	010 - 000	2 2 1 - 3 1 2
H ₂ O	6.3905	010 - 000	1 1 1 - 2 0 2
H ₂ O	6.4094	010 - 000	3 1 2 - 3 2 1
H ₂ O	6.4165	010 - 000	3 0 3 - 3 1 2
H ₂ O	6.4205	010 - 000	0 0 0 - 1 1 1
H ₂ O	6.4338	010 - 000	5 1 4 - 5 2 3
H ₂	6.4388	1 - 1	S(6)
H ₂ O	6.4848	010 - 000	2 1 2 - 2 2 1
H ₂ O	6.4925	010 - 000	2 1 2 - 3 0 3
H ₂ O	6.4978	010 - 000	1 0 1 - 2 1 2
H ₂ O	6.5195	010 - 000	3 2 1 - 3 3 0
H ₂ O	6.5226	010 - 000	3 1 3 - 3 2 2
H ₂ O	6.5423	010 - 000	3 2 2 - 3 3 1
H ₂ O	6.5554	010 - 000	4 2 3 - 4 3 2
H ₂ O	6.5676	010 - 000	2 0 2 - 3 1 3
H ₂ O	6.5738	010 - 000	4 1 4 - 4 2 3
H ₂ O	6.5904	010 - 000	3 1 3 - 4 0 4
H ₂ O	6.6287	010 - 000	4 2 3 - 5 1 4
H ₂ O	6.6421	010 - 000	1 1 0 - 2 2 1
H ₂ O	6.6723	010 - 000	1 1 1 - 2 2 0
H ₂ O	6.6836	010 - 000	4 1 4 - 5 0 5
H ₂ O	6.7078	010 - 000	4 0 4 - 5 1 5
H ₂ O	6.7123	010 - 000	6 1 6 - 6 2 5
H ₂ O	6.7235	010 - 000	2 1 1 - 3 2 2
H ₂ O	6.7745	010 - 000	5 1 5 - 6 0 6
H ₂ O	6.7865	010 - 000	5 0 5 - 6 1 6
H ₂ O	6.7934	010 - 000	3 1 2 - 4 2 3
H ₂ O	6.8265	010 - 000	2 1 2 - 3 2 1
H ₂ O	6.8531	010 - 000	4 1 3 - 5 2 4
H ₂ O	6.8577	010 - 000	2 2 0 - 3 3 1
H ₂ O	6.8642	010 - 000	2 2 1 - 3 3 0
H ₂	6.9098	0 - 0	S(5)
H ₂ O	6.9600	010 - 000	3 2 1 - 4 3 2
H ₂ O	6.9934	010 - 000	3 2 2 - 4 3 1
H ₂ O	7.0242	010 - 000	3 1 3 - 4 2 2

Table A1 *continued*

Table A1 (*continued*)

Species	Wavelength (μm)	Transition, v	Transition, J
H ₂ O	7.0451	010 – 000	3 3 1 – 4 4 0
H ₂ O	7.1182	010 – 000	5 2 3 – 6 3 4
H ₂ O	7.1471	010 – 000	4 2 3 – 5 3 2
H ₂ O	7.1647	010 – 000	4 3 1 – 5 4 2
H ₂ O	7.1714	010 – 000	4 3 2 – 5 4 1
H ₂ O	7.2079	010 – 000	4 4 1 – 5 5 0
H ₂ O	7.2726	010 – 000	4 1 4 – 5 2 3
H ₂	7.2802	1 – 1	S(5)
CH ₄	7.4748	00011F2 – 00001A1	6F2 2 – 5F1 1
CH ₄	7.4761	00011F2 – 00001A1	6F1 1 – 5F2 1
CH ₄	7.4791	00011F2 – 00001A1	6E 1 – 6F2 2
CH ₄	7.4797	00011F2 – 00001A1	6F2 1 – 5F1 2
CH ₄	7.5034	00011F2 – 00001A1	5A2 1 – 4A1 1
CH ₄	7.5044	00011F2 – 00001A1	5F2 1 – 4F1 1
CH ₄	7.5051	00011F2 – 00001A1	5E 1 – 4E 1
CH ₄	7.5070	00011F2 – 00001A1	5F1 1 – 4F2 1
CH ₄	7.5335	00011F2 – 00001A1	4F2 1 – 3F1 1
CH ₄	7.5343	00011F2 – 00001A1	4F1 1 – 3F2 1
CH ₄	7.5354	00011F2 – 00001A1	4A1 1 – 3A2 1
CH ₄	7.5634	00011F2 – 00001A1	3E 1 – 2E 1
CH ₄	7.5638	00011F2 – 00001A1	3F1 1 – 2F2 1
CH ₄	7.5940	00011F2 – 00001A1	2F2 1 – 1F1 1
CH ₄	7.6253	00011F2 – 00001A1	1A2 1 – 0A1 1
CH ₄	7.6554	00011F2 – 00001A1	6A2 1 – 6A1 1
CH ₄	7.6561	00011F2 – 00001A1	3A1 1 – 3A2 1
CH ₄	7.6570	00011F2 – 00001A1	4F1 2 – 4F2 1
CH ₄	7.6575	00011F2 – 00001A1	5F2 3 – 5F1 2
CH ₄	7.6581	00011F2 – 00001A1	1F2 1 – 1F1 1
CH ₄	7.6587	00011F2 – 00001A1	2F1 1 – 2F2 1
CH ₄	7.6590	00011F2 – 00001A1	6F2 3 – 6F1 1
CH ₄	7.6595	00011F2 – 00001A1	5E 2 – 5E 1
CH ₄	7.6603	00011F2 – 00001A1	2E 1 – 2E 1
CH ₄	7.6605	00011F2 – 00001A1	3F1 2 – 3F2 1
CH ₄	7.6628	00011F2 – 00001A1	6F1 3 – 6F2 2
CH ₄	7.6637	00011F2 – 00001A1	3F2 1 – 3F1 1
CH ₄	7.6652	00011F2 – 00001A1	4E 1 – 4E 1
CH ₄	7.6673	00011F2 – 00001A1	4F2 2 – 4F1 1
CH ₄	7.6704	00011F2 – 00001A1	4A2 1 – 4A1 1
CH ₄	7.6724	00011F2 – 00001A1	5F1 2 – 5F2 1
CH ₄	7.6759	00011F2 – 00001A1	5F2 2 – 5F1 1

Table A1 *continued*

Table A1 (*continued*)

Species	Wavelength (μm)	Transition, ν	Transition, J
CH ₄	7.6802	00011F2 – 00001A1	6A1 1 – 6A2 1
CH ₄	7.6831	00011F2 – 00001A1	6F1 2 – 6F2 1
CH ₄	7.6842	00011F2 – 00001A1	6E 2 – 6E 1
CH ₄	7.6907	00011F2 – 00001A1	0F2 1 – 1F1 1
CH ₄	7.7239	00011F2 – 00001A1	1E 1 – 2E 1
CH ₄	7.7257	00011F2 – 00001A1	1F1 1 – 2F2 1
CH ₄	7.7582	00011F2 – 00001A1	2F2 2 – 3F1 1
CH ₄	7.7612	00011F2 – 00001A1	2F1 2 – 3F2 1
CH ₄	7.7651	00011F2 – 00001A1	2A1 1 – 3A2 1
CH ₄	7.7914	00011F2 – 00001A1	3A2 1 – 4A1 1
CH ₄	7.7943	00011F2 – 00001A1	3F2 2 – 4F1 1
CH ₄	7.7965	00011F2 – 00001A1	3E 2 – 4E 1
CH ₄	7.8027	00011F2 – 00001A1	3F1 3 – 4F2 1
CH ₄	7.8280	00011F2 – 00001A1	4F2 4 – 5F1 1
CH ₄	7.8318	00011F2 – 00001A1	4F1 3 – 5F2 1
CH ₄	7.8408	00011F2 – 00001A1	4E 2 – 5E 1
CH ₄	7.8429	00011F2 – 00001A1	4F2 3 – 5F1 2
CH ₄	7.8642	00011F2 – 00001A1	5E 3 – 6E 1
CH ₄	7.8653	00011F2 – 00001A1	5F1 4 – 6F2 1
CH ₄	7.8692	00011F2 – 00001A1	5A1 1 – 6A2 1
CH ₄	7.8804	00011F2 – 00001A1	5F1 3 – 6F2 2
CH ₄	7.8841	00011F2 – 00001A1	5F2 4 – 6F1 1
CH ₄	7.8875	00011F2 – 00001A1	5A2 2 – 6A1 1
H ₂	8.0257	0 – 0	S(4)
H ₂	8.4534	1 – 1	S(4)
OH	9.1337	X1/2 0 – X1/2 0	RR 45.5ee
OH	9.1384	X1/2 0 – X1/2 0	RR 44.5ee
OH	9.1546	X1/2 0 – X1/2 0	RR 43.5ff
OH	9.1813	X1/2 0 – X1/2 0	RR 42.5ff
OH	9.2186	X1/2 0 – X1/2 0	RR 41.5ff
OH	9.2664	X1/2 0 – X1/2 0	RR 40.5ff
OH	9.3251	X1/2 0 – X1/2 0	RR 39.5ff
OH	9.3947	X1/2 0 – X1/2 0	RR 38.5ff
OH	9.4757	X1/2 0 – X1/2 0	RR 37.5ff
OH	9.5686	X1/2 0 – X1/2 0	RR 36.5ff
H ₂	9.6656	0 – 0	S(3)
OH	9.6726	X3/2 0 – X3/2 0	RR 36.5ee
OH	9.6738	X1/2 0 – X1/2 0	RR 35.5ff
OH	9.7921	X1/2 0 – X1/2 0	RR 34.5ff
OH	9.9241	X1/2 0 – X1/2 0	RR 33.5ff

Table A1 *continued*

Table A1 (*continued*)

Species	Wavelength (μm)	Transition, v	Transition, J
OH	10.0707	X1/2 0 – X1/2 0	RR 32.5ff
OH	10.0707	X1/2 0 – X1/2 0	RR 32.5ff
H ₂	10.1778	1–1	S(3)
OH	10.2329	X1/2 0 – X1/2 0	RR 31.5ff
OH	10.4120	X1/2 0 – X1/2 0	RR 30.5ff
OH	10.6093	X1/2 0 – X1/2 0	RR 29.5ff
OH	10.8263	X1/2 0 – X1/2 0	RR 28.5ff
OH	11.0475	X3/2 0 – X3/2 0	RR 28.5ff
OH	11.0522	X1/2 0 – X1/2 0	RR 27.5ee
OH	11.0647	X1/2 0 – X1/2 0	RR 27.5ff
OH	11.3267	X1/2 0 – X1/2 0	RR 26.5ff
OH	11.6103	X3/2 0 – X3/2 0	RR 26.5ee
OH	11.6147	X1/2 0 – X1/2 0	RR 25.5ff
OH	11.6147	X1/2 0 – X1/2 0	RR 25.5ff
OH	11.9314	X1/2 0 – X1/2 0	RR 24.5ff
OH	12.2556	X3/2 0 – X3/2 0	RR 24.5ff
H ₂	12.2796	0 – 0	S(2)
OH	12.6574	X3/2 0 – X3/2 0	RR 23.5ee
OH	12.6646	X1/2 0 – X1/2 0	RR 22.5ff
OH	13.0807	X3/2 0 – X3/2 0	RR 22.5ee
OH	13.0893	X1/2 0 – X1/2 0	RR 21.5ff
OH	13.5492	X3/2 0 – X3/2 0	RR 21.5ee
OH	13.5596	X1/2 0 – X1/2 0	RR 20.5ff
HCN	13.7598	0110–0000	R 4e
HCN	13.8160	0110–0000	R 3e
HCN	13.8726	0110–0000	R 2e
HCN	13.9297	0110–0000	R 1e
HCN	13.9873	0110–0000	R 0e
HCN	14.0295	0110–0000	Q 10e
HCN	14.0324	0110–0000	Q 9e
HCN	14.0350	0110–0000	Q 8e
HCN	14.0373	0110–0000	Q 7e
HCN	14.0393	0110–0000	Q 6e
HCN	14.0410	0110–0000	Q 5e
HCN	14.0425	0110–0000	Q 4e
HCN	14.0436	0110–0000	Q 3e
HCN	14.0445	0110–0000	Q 2e
HCN	14.0451	0110–0000	Q 1e
OH	14.0692	X3/2 0 – X3/2 0	RR 20.5ee
OH	14.0818	X1/2 0 – X1/2 0	RR 19.5ff

Table A1 *continued*

Table A1 (*continued*)

Species	Wavelength (μm)	Transition, v	Transition, J
HCN	14.1630	0110-0000	P 2e
HCN	14.2225	0110-0000	P 3e
HCN	14.2826	0110-0000	P 4e
CO ₂	14.5528	01101 - 00001	R 24e
CO ₂	14.5867	01101 - 00001	R 22e
CO ₂	14.6208	01101 - 00001	R 20e
OH	14.6482	X3/2 0 - X3/2 0	RR 19.5ee
CO ₂	14.6549	01101 - 00001	R 18e
OH	14.6636	X1/2 0 - X1/2 0	RR 18.5ff
CO ₂	14.6892	01101 - 00001	R 16e
CO ₂	14.7235	01101 - 00001	R 14e
CO ₂	14.7580	01101 - 00001	R 12e
CO ₂	14.7925	01101 - 00001	R 10e
CO ₂	14.8271	01101 - 00001	R 8e
CO ₂	14.8618	01101 - 00001	R 6e
CO ₂	14.8966	01101 - 00001	R 4e
CO ₂	14.9315	01101 - 00001	R 2e
CO ₂	14.9564	01101 - 00001	Q 34e
CO ₂	14.9595	01101 - 00001	Q 32e
CO ₂	14.9624	01101 - 00001	Q 30e
CO ₂	14.9652	01101 - 00001	Q 28e
CO ₂	14.9664	01101 - 00001	R 0e
CO ₂	14.9677	01101 - 00001	Q 26e
CO ₂	14.9701	01101 - 00001	Q 24e
CO ₂	14.9722	01101 - 00001	Q 22e
CO ₂	14.9742	01101 - 00001	Q 20e
CO ₂	14.9760	01101 - 00001	Q 18e
CO ₂	14.9777	01101 - 00001	Q 16e
CO ₂	14.9791	01101 - 00001	Q 14e
CO ₂	14.9803	01101 - 00001	Q 12e
CO ₂	14.9814	01101 - 00001	Q 10e
CO ₂	14.9823	01101 - 00001	Q 8e
CO ₂	14.9830	01101 - 00001	Q 6e
CO ₂	14.9835	01101 - 00001	Q 4e
CO ₂	14.9838	01101 - 00001	Q 2e
CO ₂	15.0191	01101 - 00001	P 2e
CO ₂	15.0543	01101 - 00001	P 4e
CO ₂	15.0896	01101 - 00001	P 6e
CO ₂	15.1249	01101 - 00001	P 8e
CO ₂	15.1604	01101 - 00001	P 10e

Table A1 *continued*

Table A1 (*continued*)

Species	Wavelength (μm)	Transition, v	Transition, J
CO ₂	15.1959	01101 – 00001	P 12e
CO ₂	15.2316	01101 – 00001	P 14e
CO ₂	15.2673	01101 – 00001	P 16e
OH	15.2674	X3/2 0 – X3/2 0	RR 18.5ff
CO ₂	15.3031	01101 – 00001	P 18e
CO ₂	15.3390	01101 – 00001	P 20e
CO ₂	15.3749	01101 – 00001	P 22e
OH	16.0214	X3/2 0 – X3/2 0	RR 17.5ee
OH	16.0451	X1/2 0 – X1/2 0	RR 16.5ff
OH	16.8404	X3/2 0 – X3/2 0	RR 16.5ee
OH	16.8703	X1/2 0 – X1/2 0	RR 15.5ff
H ₂	17.0362	0 – 0	S(1)
OH	17.7693	X3/2 0 – X3/2 0	RR 15.5ee
OH	17.8076	X1/2 0 – X1/2 0	RR 14.5ff
OH	18.7921	X3/2 0 – X3/2 0	RR 14.5ff
OH	18.8299	X3/2 0 – X3/2 0	RR 14.5ee
OH	18.8487	X1/2 0 – X1/2 0	RR 13.5ee
OH	18.8795	X1/2 0 – X1/2 0	RR 13.5ff
OH	20.0085	X3/2 0 – X3/2 0	RR 13.5ff
OH	20.0497	X3/2 0 – X3/2 0	RR 13.5ee
OH	20.0819	X1/2 0 – X1/2 0	RR 12.5ee
OH	20.1151	X1/2 0 – X1/2 0	RR 12.5ff
OH	21.4199	X3/2 0 – X3/2 0	RR 12.5ff
OH	21.4649	X3/2 0 – X3/2 0	RR 12.5ee
OH	21.5169	X1/2 0 – X1/2 0	RR 11.5ee
OH	21.5525	X1/2 0 – X1/2 0	RR 11.5ff
OH	23.0739	X3/2 0 – X3/2 0	RR 11.5ff
OH	23.1234	X3/2 0 – X3/2 0	RR 11.5ee
OH	23.2048	X1/2 0 – X1/2 0	RR 10.5ee
OH	23.2433	X1/2 0 – X1/2 0	RR 10.5ff
OH	25.0351	X3/2 0 – X3/2 0	RR 10.5ff
OH	25.0899	X3/2 0 – X3/2 0	RR 10.5ee
OH	25.2164	X1/2 0 – X1/2 0	RR 9.5ee
OH	25.2579	X1/2 0 – X1/2 0	RR 9.5ff

B. H₂ ROTATIONAL DIAGRAMSC. CO₂ AND ¹³CO₂ RATIO MAPS

To further investigate the nature of the hole in the ¹³CO₂ absorption, we examine the CO₂/¹³CO₂ ratio in HOPS 370's envelope. We generated a ¹³CO₂ column density map using a band strength (density-corrected), $A = 1.15 \times 10^{-16}$ cm/mol (Gerakines et al. 1995; Bouilloud et al. 2015, similar to the CO₂ column density map discussed in Section

Table A2. Detected Atomic and Ionic lines. Line information is taken from NIST (Kramida & Ralchenko 1999)

Species	Wavelength (μm)	Transition
[Fe II]	5.341	$^4F_{9/2} - ^6D_{9/2}$
[Ni II]	6.635	$^2D_{3/2} - ^2D_{5/2}$
[Fe II]	6.7235	$^4F_{9/2} - ^6D_{7/2}$
[Ar II]	6.985	$^2P_{1/2} - ^2P_{3/2}$
[Co II]	10.523	$^3F_3 - ^3F_4$
[Ni II]	10.682	$^4F_{7/2} - ^4F_{9/2}$
[Cl I]	11.333	$^2P_{1/2} - ^2P_{3/2}$
[Ni II]	12.729	$^4F_{5/2} - ^4F_{7/2}$
[Ne II]	12.814	$^2P_{1/2} - ^2P_{3/2}$
[Fe II]	17.936	$^4F_{7/2} - ^4F_{9/2}$
[Fe II]	24.522	$^4F_{5/2} - ^4F_{7/2}$
[S I]	25.245	$^3P_1 - ^3P_2$
[Fe II]	25.985	$^6F_{7/2} - ^6F_{9/2}$

4.2). The column density ratio map of $\text{CO}_2/^{13}\text{CO}_2$ is shown in the top panel of Figure C2. We calculated the mean molecular ratios of $\text{CO}_2/^{13}\text{CO}_2$ in the aperture marked by magenta and black colors at the shocked knot and the continuum peak in Figure C2, yielding values of 63.5 ± 9.8 and 62.0 ± 8.9 , respectively. Moving away from the shocked knot in both the north and south directions, we observed a decreasing trend in the $\text{CO}_2/^{13}\text{CO}_2$ ratios (see bottom panel of Figure C2).

The $\text{CO}_2/^{13}\text{CO}_2$ ratio can vary depending on the band strengths used in the column density calculation. Figure C2 (bottom panel) compares ratios calculated with band strengths from Gerakines et al. 1995 (density-corrected values; shown in multiple colors) and Bouilloud et al. 2015 (in gray; $A = 6.8 \times 10^{-17}$ cm/mol for CO_2 and $A = 7.6 \times 10^{-17}$ cm/mol for $^{13}\text{CO}_2$). The mean ratio difference between the two sets is a factor of 1.17. For this discussion, we adopt the density-corrected band strengths of Gerakines et al. 1995 as Bouilloud et al. 2015 suspected that their band strength values are lower due to possible saturation of 4.27 CO_2 absorption feature. For a detailed discussion on the band strength uncertainties, the reader is referred to Brunken et al. (in prep).

The obtained molecular ratios of $\text{CO}_2/^{13}\text{CO}_2$ in HOPS 370's envelope, closer to the continuum peak and shocked knot, are similar to the average local ISM ratio of 69 (Boogert et al. 2000), as well as the local dark cloud ratio of 69–87 measured in the Chameleon I star-forming region (McClure et al. 2023). However, farther from the continuum peak and shocked knot the ratio decreases by a factor of $\sim 1.3 - 1.7$. It is worth noting that Boogert et al. 2000 reported variations in the $\text{CO}_2/^{13}\text{CO}_2$ ratio in some sources. Along the lines of sight toward GC 3, W 33A, and HH 100, they measured low $\text{CO}_2/^{13}\text{CO}_2$ ratios of 52, 53, and 52, respectively.

Alternatively, the variation in the ratio may result from radiative transfer effects. Sturm et al. 2023 suggested that the saturation of the main isotopologue of CO_2 ice absorption band by scattered light could lead to a lower $\text{CO}_2/^{13}\text{CO}_2$ ratio. They observed a molecular ratio of 14 in the edge-on protoplanetary disk HH 48 NE. As mentioned in Section 3, our optical depth calculations also utilize scattered light as a background continuum. Therefore, it is plausible that low $\text{CO}_2/^{13}\text{CO}_2$ ratios farther away from the central protostar in our observations may be attributed to the partial saturation of the CO_2 main isotopologue. This can lower the observed optical depth of the CO_2 feature, resulting in an underestimate of the column density in the protostellar envelope.

Despite this potential issue with the CO_2 optical depth. The presence of the low opacity hole is clearly supported by other evidence. The hole is seen in multiple ice including $^{13}\text{CO}_2$ and H_2O . In addition, the independent extinction measurement using H_2 rotational lines agrees with the low extinction at the shocked knot position.

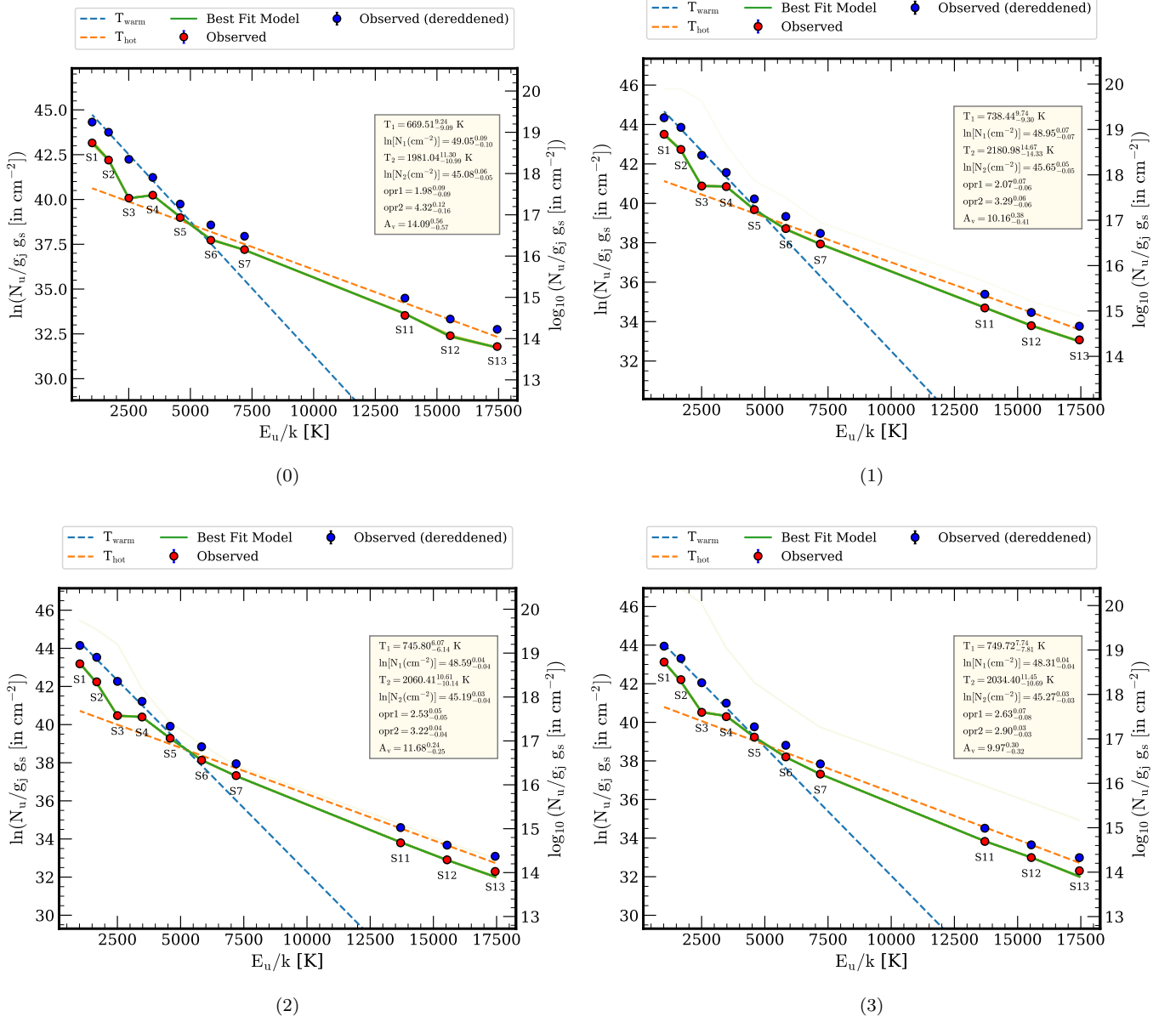


Figure B1. H_2 rotational diagram for apertures 0, 1, 2, and 3 displayed in Figure 10. Red points are the observed data points while the blue points are de-reddened points using the KP5 extinction law. Blue and orange dashed lines correspond to cold and hot temperature gas considered in the fitting model. The green line is the best fit for the observed rotational diagram.

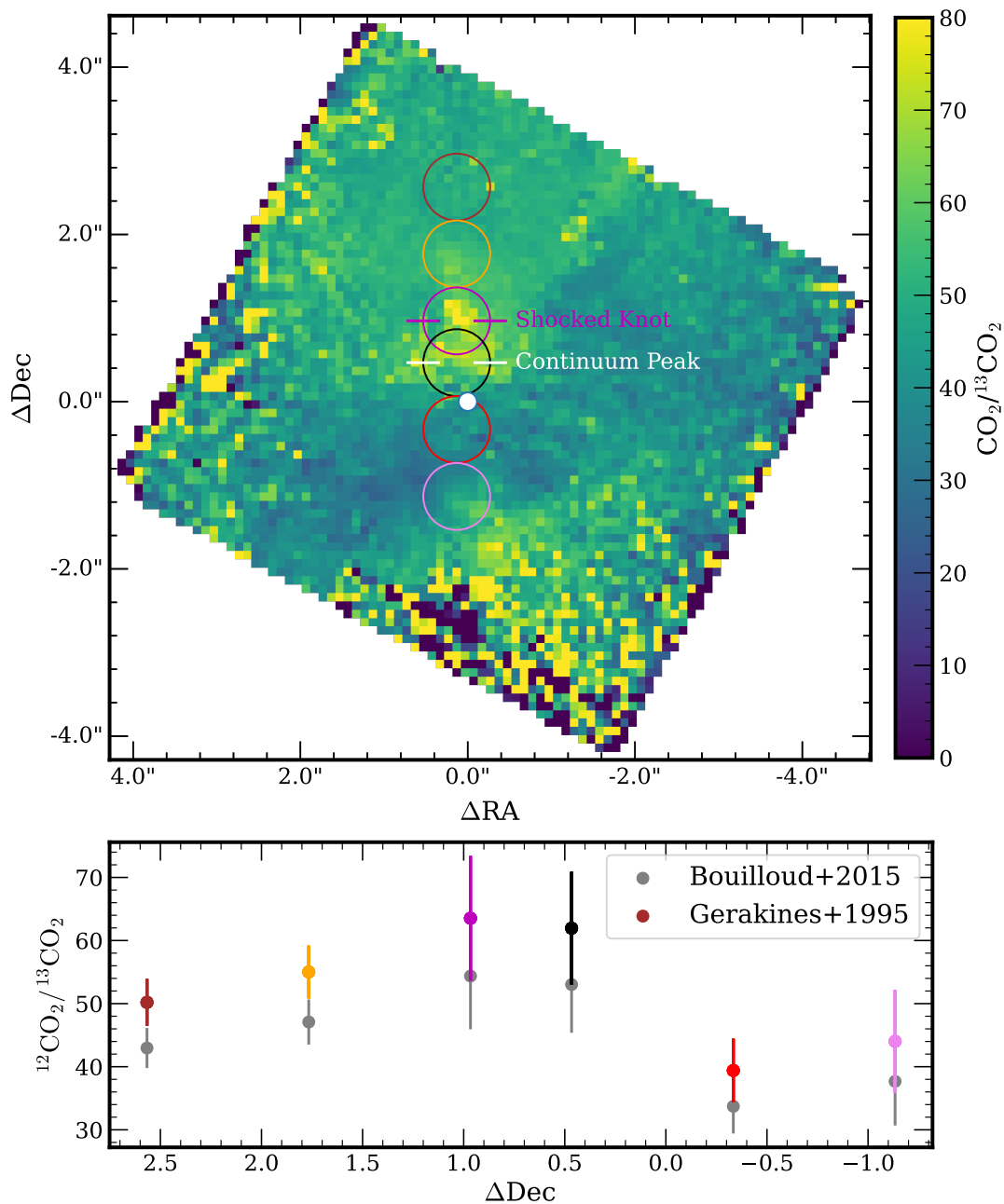


Figure C2. *Top panel:* CO_2 ($4.27\ \mu\text{m}$) to $^{13}\text{CO}_2$ ($4.38\ \mu\text{m}$) ratio map. Shocked knot and continuum peaks are marked by magenta and white color lines, respectively. Colored apertures marked on the map are used to calculate the mean $\text{CO}_2/^{13}\text{CO}_2$ ratio plotted in the bottom panel. *Bottom panel:* Mean $\text{CO}_2/^{13}\text{CO}_2$ ratio of marked apertures in the top panels as a function of the angular distance of aperture from the ALMA continuum position. Multi-colored and gray markers represent ratio values calculated using the density corrected band strength values from Gerakines et al. 1995, and Bouilloud et al. 2015, respectively.